

# Terahertz polarization converters: physical principles, design, and applications

A.K. Kaveev, G.I. Kropotov

DOI: <https://doi.org/10.3367/UFNe.2024.09.039770>

## Contents

|  |            |
|--|------------|
| <b>1. Introduction</b>   | <b>294</b> |
| <b>2. Simple THz polarization converters</b>   | <b>295</b> |
| 2.1 Film polarizers; 2.2 Wire grid polarizers; 2.3 Monochromatic waveplates; 2.4 Other polarization converters |            |
| <b>3. Polarizer-based devices</b>  | <b>303</b> |
| 3.1 Achromatic waveplates; 3.2 Composite tunable phase-delay waveplates; 3.3 Terahertz polarization filters    |            |
| <b>4. Conclusions</b>  | <b>313</b> |
| <b>References</b>  | <b>313</b> |

**Abstract.** The paper examines the basic physical principles of the operation of terahertz (THz) polarization converters and discusses the main types of polarizers, including those based on wire grids, films, metamaterials, etc. More sophisticated devices based on polarizers made of stacks of segmented, achromatic, and tunable composite waveplates, including those operating over a wide wavelength range, and on THz polarization filters are considered. The basic principles of their calculation using the Jones formalism are described.

**Keywords:** THz polarimetry, waveplates, retardation, quartz optics, Jones formalism

## 1. Introduction

The terahertz (THz) frequency range (100 GHz–10 THz) covers a significant part of the optical spectrum between the microwave and infrared bands. Unlike the latter, the THz frequency range has been quite underdeveloped for a long time, due to the lack of both sources of high-power THz radiation and receivers capable of registering radiation in this region of the spectrum. Interest in THz radiation is associated with the prospects for its application in the field of telecommunications for ultra-dense, secure transmission of information; for internal and external communication in integrated circuits; in the field of spectroscopy—chemical characterization of the composition of complex compounds (since many vibrational and rotational levels of large organic molecules lie in the THz range); in security and alarm systems;

and for the detection of weapons, explosives, and drugs [1–5]. The use of THz radiation in tomography and medicine is also very promising [4, 6]. Rapid progress in the field of THz optoelectronics over the past 15–20 years has required the development of production of optical components that correspond to the features of devices for this spectral range.

Polarization optics is a branch of physics that studies polarization phenomena in birefringent crystals. Polarimetry is a separate subfield related to the analysis of polarization of the radiation under study. Polarimetry, along with spectroscopy, is of great importance for the analysis of THz radiation, since polarization is also a parameter characterizing light.

Terahertz time-domain spectroscopy (THz-TDS) is one of the main techniques for studying transmission of various objects in the THz wavelength range. Terahertz time-domain spectroscopy can be used to examine optical properties, such as the complex refractive index, absorption coefficient, complex permittivity, and complex conductivity of an object [7]. However, polarization, which is also an important characteristic of electromagnetic waves, has received little attention in THz-TDS for a long time. In order to characterize polarization properties of objects, use is made of terahertz time-domain polarimetry (THz-TDP), where a set of polarizers and waveplates is incorporated into a standard THz-TDS spectrometer [8].

Crystalline quartz is a traditional material in THz instrumentation. This material is excellent for THz applications due to its transmittance of more than 70% in the range from 40  $\mu\text{m}$  and below. In addition, crystalline quartz is a birefringent material [9], which allows it to be used in polarization THz optics to develop elements that convert polarization of incident radiation. Note that any other material—birefringent and transparent in the THz range, such as sapphire or boron nitride—can be selected as an alternative. A technological challenge in the latter case is the necessity of locating the birefringent axis in the plane of the waveplates.

This review discusses main passive optical elements that convert polarization of THz radiation. Section 2 considers

A.K. Kaveev<sup>(1,\*), G.I. Kropotov<sup>(2)</sup></sup>

<sup>(1)</sup> Ioffe Institute, Russian Academy of Sciences, ul. Politekhnicheskaya 26, 194021 St. Petersburg, Russian Federation

<sup>(2)</sup> Tydex LLC, ul. Domostroitel'naya 16, 194292 St. Petersburg, Russian Federation  
E-mail: <sup>(\*)</sup> kaveev@mail.ioffe.ru

Received 1 May 2024, revised 28 July 2024  
*Uspekhi Fizicheskikh Nauk* 195 (3) 311–333 (2025)  
Translated by A.I. Ulitkin

simple passive elements, such as film and wire grid polarizers and waveplates. In addition, segmented waveplates and several more exotic cases of polarizers are described. Section 3 discusses more sophisticated multicomponent polarization converters, including achromatic waveplates, polarization filters, and tunable polarization converters.

## 2. Simple THz polarization converters

Depending on the type of polarization obtained, simple polarizers are divided into linear, circular, and elliptical. Circular and elliptical polarizers, as a rule, contain a linear polarizer and so-called crystal phase plates. The operating principle of a linear polarizer is based on dividing light with an arbitrary degree of polarization into two orthogonal components, where one polarization component is transmitted by the polarizer and the other is deflected or absorbed. To split light into components, one of the following phenomena is generally used: double refraction, reflection or refraction of light at the boundaries of dielectrics (the Brewster effect), dichroism, and polarizing properties of narrow slits and small-period gratings. Birefringent polarizers are made in the form of crystalline prisms, for example, from Iceland spar (these include Nicol, Glan–Foucault, and other prisms). These polarizers, when made of crystalline quartz or sapphire, find application in the THz range. Examples of dichroic polarizers in the THz range include anisotropic film and wire grid polarizers, discussed below.

Polarizers generally allow radiation of arbitrary polarization to be converted into polarized or partially polarized light, which makes them an integral part of THz optical circuits. At present, a number of exotic cases of THz polarizers are known, including those based on liquid crystals (to be discussed below), carbon nanotubes [10, 11], graphene-based chains and resonators [12, 13], and aluminum films deposited on silicon at a Brewster angle [14]. However, substrate-less wire grid or film polarizers are more common. Polarization characteristics of polarizers of various types are measured using spectroscopic techniques. They can be Fourier spectroscopy or pulsed THz spectroscopy. A schematic of polarization measurements for the latter is shown in Fig. 1a.

In polarized light from the source, time forms are measured in two perpendicular positions of the polarizer: with the highest and lowest levels of signal transmission.

### 2.1 Film polarizers

For operation in the far-IR and THz spectral ranges, use is made of propylene film-based polarizers (Fig. 1b). The film usually has sine-shaped grooves, although another profile is also acceptable, for example, sawtooth-shaped, with part of the groove having an aluminum coating. From a physical point of view, almost any groove profile is suitable, since the geometric size of the profile is approximately 10–1000 times smaller than the wavelength of the THz range, and there are no significant edge effects. The sine-shaped profile is the easiest to manufacture technologically and is formed using a chalcogenide photoresist. As a result, the polarizer operates as a transmission diffraction grating. Typical applications of film polarizers include THz microscopy, molecular orientation studies of crystalline and polymer films, imaging optics, THz sensors and detectors, Fourier spectroscopy, and THz spectroscopic studies. Distinctive properties of film polarizers include the use of mid-IR-to-THz wavelengths in a very wide spectral range, high transmission in the far-IR and THz

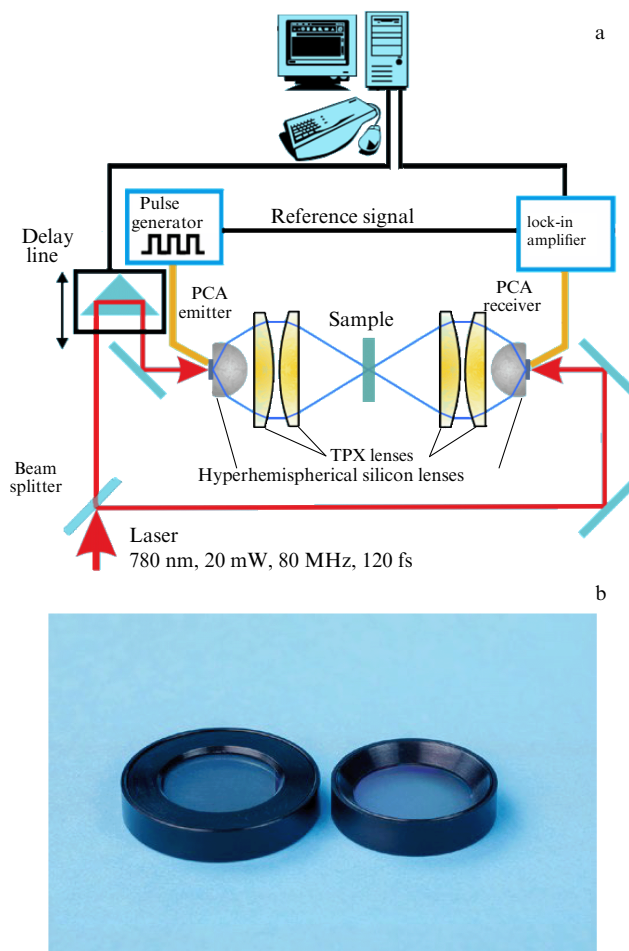


**Figure 1.** (a) Schematic of a setup for studying characteristics of polarizers (borrowed through private communications with Tydex LLC), and (b) film polarizer (borrowed from [15]).

spectral region, and a high degree of polarization of transmitted radiation.

Film polarizers are characterized by a number of parameters, such as effective transmittance  $K_1$ , unwanted polarization transmittance  $K_2$ , degree of polarization  $P_1 = (K_1 - K_2)/(K_1 + K_2)$ , and extinction coefficient  $E = K_1/(2K_2)$  (or logarithmic extinction coefficient  $E = 10 \lg(K_1/K_2)$ , [dB]). The degree of polarization and the extinction coefficient are determined through the transmittances of useful and parasitic polarization. As an example, Fig. 2 shows the transmission spectra of (a) useful and (b) parasitic polarizations and (c) the degree of polarization of polarizers. The spectra were measured using two instruments: a Bruker Vertex 70 Fourier spectrometer in the short-wavelength range from 0.9  $\mu\text{m}$  to 670  $\mu\text{m}$  (from 333.1 THz to 0.45 THz) and a Menlo Systems Tera-K8 THz time-domain spectrometer with a 600- $\mu\text{m}$  dipole antenna ( $f_c = 0.5$  THz) in the long-wavelength range from 250  $\mu\text{m}$  to 3000  $\mu\text{m}$ .

Figure 2d shows the spectral dependence of the extinction coefficient of output radiation. As examples, we present characteristic parameters obtained in the range from 15 to 3000  $\mu\text{m}$  [15]:  $K_1 > 80\%$ ,  $K_2 < 0.002\%$ ,  $P_1 > 99.99$ ,  $E > 47$  dB. The polarizers shown in Fig. 2 were fabricated by applying aluminum strips to a 30- $\mu\text{m}$ -thick polypropylene substrate. The shape of the grooves is sinusoidal, the concentration of grooves is 1200/mm, the thickness of one

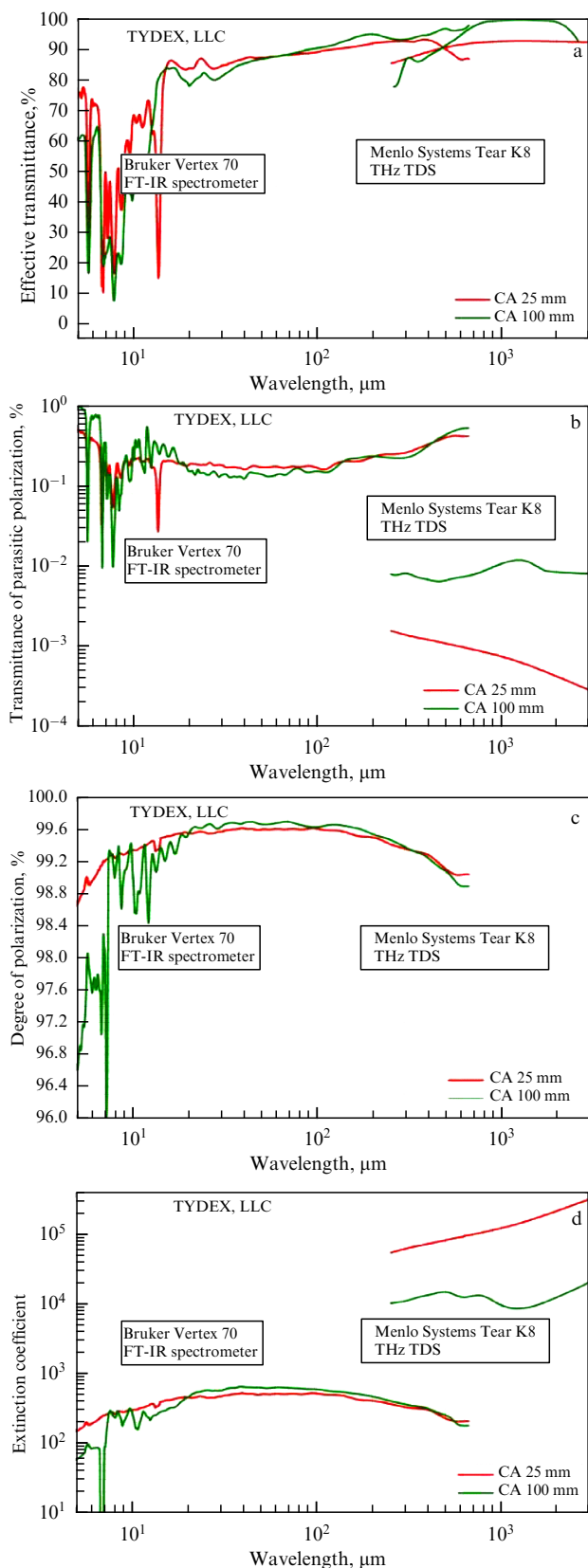


**Figure 2.** Spectral dependence of transmittance of (a) useful and (b) parasitic polarizations of polypropylene polarizers with an aperture of 25 mm and 100 mm. (c) Degree of polarization of these polarizers. Break in transmission curves appears due to different dynamic ranges of spectrometers, which affect noise signal level. (d) Spectral dependence of extinction coefficient. (Borrowed from [15].)

groove is 100 nm, the width is 400–500 nm, and the free aperture is 25–100 mm.

## 2.2 Wire grid polarizers

If the power of incident radiation is high, film polarizers cannot be employed. In this case, wire grid polarizers, designed to polarize radiation from 150  $\mu\text{m}$  to centimeter wavelengths, are used to operate in the microwave and THz frequency ranges. They are made of parallel tungsten wires (usually about 10  $\mu\text{m}$  in diameter) mounted in a holder without a substrate. Such polarizers are usually applied, along with film polarizers, in THz spectroscopy and microscopy, sensors and detectors, Fourier spectroscopy, and THz and microwave polarimetry. However, in addition to this, a high damage threshold allows wire grid polarizers to be used with free-electron lasers, gyrotrons, accelerators, and other high-power THz radiation sources. These polarizers are resistant to high energies of polarized radiation, and, due to the absence of a substrate, they provide high transmission of desired polarization at its high degree. In addition, other types of polarizers do not make it possible to avoid losses, since there will always be reflection from the substrate and absorption loss in the substrate. This leads to the fact that part of the desired polarization is reflected and absorbed in the substrate, which affects the efficiency of the device. Wire grid polarizers are devoid of this drawback due to the absence of any substrate.

Wire grid polarizers demonstrate reflectance and transmittance that are close to 100% for the corresponding polarization planes in the spectral range from close-to-zero frequencies to frequencies  $c/2d$  [Hz], where  $1/d$  is the spatial frequency of the wires [16]. To describe the spectral range in which wire grid polarizers operate effectively, use is made of the parameter  $\chi = d/\lambda$ , where  $d$  is the wire grid period and  $\lambda$  is the wavelength. Another advantage of wire grid polarizers is their ability to reflect radiation of a certain polarization at the required angle. This property is used, for example, in certain configurations of Fourier interferometers [16, 17].

The method of fabricating wire grid polarizers with significant parameters is of great importance. Vickers et al. [16] were the first to manufacture a wire grid polarizer. They employed a coil-winder, of the type used to prepare transformer coils, to wind the wire. Use was made of stainless steel wire with a diameter of 50  $\mu\text{m}$  and a clamping mechanism to secure the wire, providing it with the required tensile strength. Costley et al. [18] used a modified commercially available apparatus to wind wire. The polarizers were made of 10- $\mu\text{m}$  tungsten wire using a modified commercially available coil-winder. After winding, the wires were fixed to the holder, previously placed inside the bobbin holder, using glue (amyl acetate diluted in acetone), and then cut. Costley et al. [18] also noted that the described coil-winder makes it possible to manufacture grids with a minimum period of 25  $\mu\text{m}$  (a maximum period of 1.8 mm) and with a usable aperture up to 120 mm in diameter. There is also a method that allows wire to be wound without using a coil-winder, i.e., manually. Sentz et al. [19] described this method, which involves the use of grooves applied to both sides of the winding holder, controlling the winding period. Sentz et al. [19] used stainless steel wire with a diameter of 50  $\mu\text{m}$ , which was wound with a spacing of 175  $\mu\text{m}$ , and tungsten wire with a diameter of 30 and 10  $\mu\text{m}$  with a spacing of 90 and 122  $\mu\text{m}$ , respectively. Shapiro and Bloemhof [20] described a more modern coil winding technique, which uses an apparatus



**Figure 3.** Wire grid polarizer with variable angular position of wire (borrowed from [22]).

similar to that in [18]. The only difference is that the winding spacing was monitored using a pre-programmed algorithm in the program that controlled the movement of the wire-feeding part of the coil-winder. Shapiro and Bloemhof [20] used 10- $\mu\text{m}$ -diameter tungsten wire, coated with gold, wound at a speed of 17 revolutions per minute and with a period of 40  $\mu\text{m}$ . Subsequent papers described only an improvement in the coil-winding machine of increasing the aperture without significant changes to the design of the apparatus or transferring wire to the holder. For example, Hu et al. [21] used 100- $\mu\text{m}$ -diameter molybdenum wire, which was wound at a speed of 8 revolutions per minute and with a period of 300  $\mu\text{m}$ . They note that in this approach it is possible to manufacture polarizers with a maximum aperture of 500 mm at a minimum wire diameter of 80  $\mu\text{m}$  with a spacing of 100  $\mu\text{m}$ .

Tydex LLC [22] developed a method for fabricating wire grid polarizers at an increased speed and length of the winding area by using improved control of the period and monitoring wire tension during winding. The essence of the method is that tungsten wire is wound with a winder at a speed, period, and winding width pre-programmed in a computer program. The wire tension is controlled by an electronic indicator on the apparatus. After winding, the resulting structure is transferred from the winding holder to a round working holder using a gluing stand, and the holder is given a marketable appearance using stands for cutting wire. The free aperture of such polarizers is 36–136 mm, the polarizers are made of 11- $\mu\text{m}$ -diameter tungsten wire, and the spacing between the wires is 16  $\mu\text{m}$ . The manufactured polarizers operate in a range up to 6, 3, and 2 THz, provided the extinction coefficient is > 10, > 20, and > 30 dB, respectively. As examples, we can present characteristic parameter values obtained at Tydex [23] in the range from 15 to 3000  $\mu\text{m}$ :  $K_1 > 92\%$ ,  $K_2 < 0.1\%$ ,  $E > 30$  dB (Figs 3 and 4).

Currently, there is no ready solution to Maxwell’s equations describing the response of THz film (grooved) or wire grid polarizers. At the same time, a number of papers (for example, [23, 24]) describe an approach to calculating transmittance of periodic metal structures. The authors of papers [25, 26] presented the effective medium theory (EMT), which allows one to evaluate optical characteristics of devices based on metal gratings. The effective medium theory is used to determine the effective

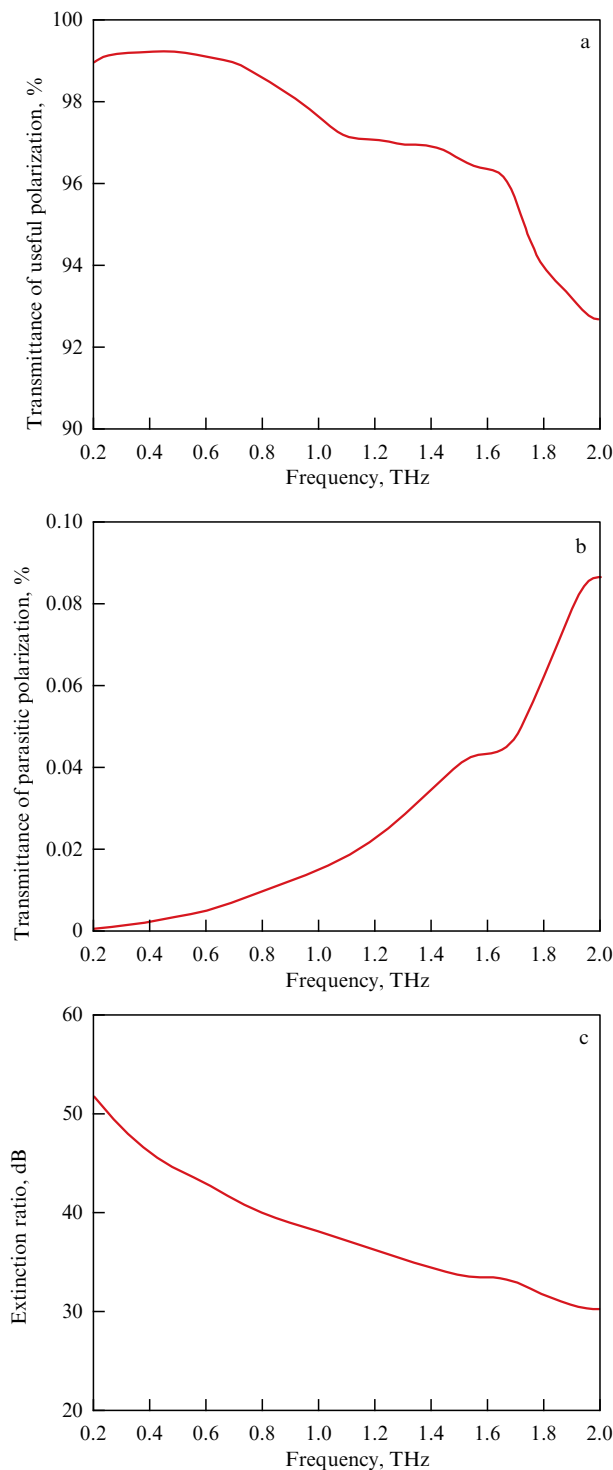


**Figure 4.** Spectral dependence of transmittance of (a) useful and (b) parasitic polarizations of a wire grid polarizer. (c) Spectral dependence of extinction coefficient. (Borrowed from [22].)

permittivity of periodic structures when developing various optical filters [27, 28] and diffractive optical elements [29]. This theory is also applicable in calculating photonic crystals (see, for example, [30]) and in developing negative-index metamaterials (see, for example, [31]). According to the EMT, a periodic structure or grating can be considered from the point of view of diffraction, and it can be replaced by an artificial anisotropic homogeneous medium if only the zeroth order of diffraction is taken into

account, and higher orders are neglected. The grating is considered thick enough to exclude direct passage of light.

In the EMT, a simple expression is derived for the effective permittivity of the TE- and TM-polarization components in the quasi-static (long-wavelength) limit  $\Lambda \ll \lambda$ , where  $\Lambda$  and  $\lambda$  are the grating period and the wavelength of incident radiation, respectively:

$$\begin{aligned} \varepsilon_{\text{eff,TE}}^{(2)} &= \varepsilon_{0,\text{TE}} + \frac{\pi^2}{3} f^2 (1-f)^2 (\varepsilon_A - \varepsilon_B)^2 \left(\frac{\Lambda}{\lambda}\right)^2, \\ \varepsilon_{\text{eff,TM}}^{(2)} &= \varepsilon_{0,\text{TM}} + \frac{\pi^2}{3} f^2 \left(\frac{1}{\varepsilon_A} - \frac{1}{\varepsilon_B}\right)^2 \varepsilon_3^3 \varepsilon_{0,\text{TE}} \left(\frac{\Lambda}{\lambda}\right)^2, \end{aligned} \quad (1)$$

where  $f$  is the grating volume filling factor, and  $\varepsilon_A$  and  $\varepsilon_B$  are the relative permittivities of the grating materials. The zero-order permittivities  $\varepsilon_0$  in the system of Eqns (1) are determined by the expressions

$$\begin{aligned} \varepsilon_{0,\text{TE}} &= f\varepsilon_A + (1-f)\varepsilon_B, \\ \varepsilon_{0,\text{TM}} &= \frac{\varepsilon_A \varepsilon_B}{f\varepsilon_B + (1-f)\varepsilon_A} \end{aligned} \quad (2)$$

for the TE- and TM-polarization components, respectively.

Unfortunately, one of the limitations of the EMT is that it is difficult to accurately determine the effective permittivity of a metal grating by analytical expressions (1) and (2), and calculations using the EMT lead to a significant deviation of the calculated values from the experimental ones due to the large negative real part of the metal permittivity associated with high absorption. For this reason, the application of the EMT is mainly limited to structures based on dielectric materials.

Moon and Kim [23] described a more successful approach, which involves finding effective permittivities of the effective medium of a periodic structure using a modified EMT method and rigorous coupled wave analysis (RCWA) simulating a simple grating equivalent by an effective homogeneous anisotropic medium. Both methods ensure subsequent fitting of the calculated result to the wavelength dependence of the system transmission, calculated using the Fresnel coefficients. RCWA, also known as the Fourier modal method, is well suited to simulating the optical response of periodic surface-relief structures and has been successfully applied for numerical calculations to experimentally interpret obtained optical characteristics. In paper [23], RCWA is implemented in such a way that it allows Maxwell's equations to be reduced to a simple algebraic eigenvalue problem (see, for example, [32]). The fitting is based on binary search and simulated annealing to obtain optimal values of the effective permittivity (for more details on this algorithm, see below in Section 3).

Let us consider a simple tungsten grating formed by rectangular rods deposited on a silicon substrate. In order to take into account only the zeroth diffraction order, the grating period must satisfy the condition  $n_{\text{sub}} \Lambda \ll \lambda$ , where  $n_{\text{sub}}$  is the refractive index of the substrate (silicon). In addition, the grating thickness  $d_g$  should be large enough not to produce surface effects such as surface plasmon resonance. Moon and Kim [23] performed simulation for  $\lambda = 4\text{--}20 \mu\text{m}$ , i.e., for the IR region. If there is an effective medium such that the grating shown in Fig. 5a is functionally

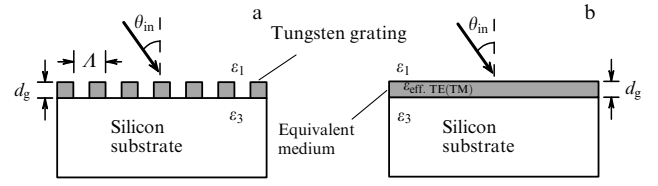


**Figure 5.** Replacement of metal grating with equivalent homogeneous medium. (a) Profile of original tungsten grating with period  $\Lambda$  and thickness  $d_g$  on a silicon substrate. (b) Optically equivalent homogeneous anisotropic film of thickness  $d_g$  located on same substrate. Beam is incident at an angle of  $\theta_{\text{in}}$ , and  $\varepsilon_1$  and  $\varepsilon_3$  are the permittivities of air and the silicon substrate, respectively. (Borrowed from [23].)

equivalent to an effective homogeneous anisotropic medium with reflectance  $R$  (Fig. 5b), then its value can be calculated using the Fresnel coefficients:

$$R_{\text{TE(TM)}} = \frac{\left| r_{1,\text{TE(TM)}} \exp(i\delta_{\text{TE(TM)}}) + r_{2,\text{TE(TM)}} \exp(-i\delta_{\text{TE(TM)}}) \right|^2}{\left| \exp(i\delta_{\text{TE(TM)}}) + r_{1,\text{TE(TM)}} r_{2,\text{TE(TM)}} \exp(-i\delta_{\text{TE(TM)}}) \right|^2}, \quad (3)$$

$$r_{1,\text{TE}} = \frac{\sqrt{\varepsilon_1} \cos \theta_1 - \sqrt{\varepsilon_{\text{eff,TE}}} \cos \theta_2}{\sqrt{\varepsilon_1} \cos \theta_1 + \sqrt{\varepsilon_{\text{eff,TE}}} \cos \theta_2},$$

$$r_{2,\text{TE}} = \frac{\sqrt{\varepsilon_{\text{eff,TE}}} \cos \theta_2 - \sqrt{\varepsilon_3} \cos \theta_3}{\sqrt{\varepsilon_{\text{eff,TE}}} \cos \theta_2 + \sqrt{\varepsilon_3} \cos \theta_3},$$

$$r_{1,\text{TM}} = \frac{\sqrt{\varepsilon_1} / \cos \theta_1 - \sqrt{\varepsilon_{\text{eff,TM}}} / \cos \theta_2}{\sqrt{\varepsilon_1} / \cos \theta_1 + \sqrt{\varepsilon_{\text{eff,TM}}} / \cos \theta_2},$$

$$r_{2,\text{TM}} = \frac{\sqrt{\varepsilon_{\text{eff,TM}}} / \cos \theta_2 - \sqrt{\varepsilon_3} \cos \theta_3}{\sqrt{\varepsilon_{\text{eff,TM}}} / \cos \theta_2 + \sqrt{\varepsilon_3} \cos \theta_3},$$

$$\delta_{\text{TE(TM)}} = 2\pi d_g (\varepsilon_{\text{eff,TE(TM)}})^{1/2} \frac{\cos \theta_2}{\lambda}.$$

The value of  $R$  calculated in this way should correspond to the results obtained using RCWA. It is important to take into account that

$$\varepsilon_{\text{eff,TE(TM)}} = (n_{\text{eff,TE(TM)}} + ik_{\text{eff,TE(TM)}})^2. \quad (4)$$

In the equation for  $R$  (3),  $r_{1,\text{TE(TM)}}$  and  $r_{2,\text{TE(TM)}}$  denote the Fresnel reflection coefficients for the polarization component TE(TM) between the air medium and the effective grating-equivalent medium, respectively, and between the effective grating-equivalent medium and the silicon substrate, respectively. The angle  $\theta_i$  ( $i = 1, 2, 3$ ) is the angle of incidence in the air, effective medium, and substrate, respectively) obeys Snell's law. At the initial stage of fitting, normal incidence of light is considered, and the fitting procedure is based on a binary search through enumeration of all possible combinations of  $n_{\text{eff,TE(TM)}}$  and  $k_{\text{eff,TE(TM)}}$  in a given range for an optimal pair that minimizes the deviation from the result obtained by RCWA. The simulated annealing algorithm was also used.

Moon and Kim [23] managed to find the dependence of  $n_{\text{eff,TE(TM)}}(\lambda)$  and  $k_{\text{eff,TE(TM)}}(\lambda)$  in the range of  $\lambda = 4\text{--}20 \mu\text{m}$  using both the modified EMT method and RCWA. At the same time, they showed that even a small variation in the calculated parameters leads to a significant discrepancy between the results obtained by the two specified methods, and scaling the obtained results to a longer-wavelength range

will lead to gross computational errors. Thus, the behavior of the spectral response (transmission and reflection) of THz wire grid polarizers has not yet been simulated. This simulation is a separate problem, the approach to solving which is possible both by the modified EMT method and RCWA, but is beyond the scope of this review. We can limit ourselves to a qualitative assertion that the operating range of the THz wire grid polarizer corresponds to the condition  $\chi \ll 1$  for the parameter  $\chi = d/\lambda$ . This is confirmed by an increase in the transmission of a parasitic wave by the THz polarizer with increasing frequency (decreasing wavelength), shown in Fig. 4b.

The described approach was also used to calculate IR wire grid polarizers [33].

### 2.3 Monochromatic waveplates

Another widely known polarization conversion method relies on the use of birefringent materials. A birefringent plate with the cut planes directed parallel to the optical axis allows elliptically polarized light to be obtained from linearly polarized light. The plate (called a waveplate or a phase plate) forms a certain phase difference between orthogonal linearly polarized components of radiation and has two orthogonal directions, one of which corresponds to the optical axis. As was mentioned above, ordinary and extraordinary waves propagate at different velocities, while maintaining their polarization. Let a linearly polarized light wave (passing through a wire grid or film polarizer in the case of THz radiation) be incident on this plate. The electric field vector  $\mathbf{E} = \mathbf{E}_0 \exp(i(\omega t - kz))$  is directed at an angle  $\alpha$  to the optical axis (we will denote it by  $\xi$ ) of the phase plate. Let us put the  $z$ -axis perpendicular to the plate, i.e., the light is incident normally. At the input to the plate, the orthogonal components  $E_\xi$  and  $E_\eta$  (in the plane of the plate) have the same oscillation phase, whereas inside the plate

$$\begin{aligned} E_\xi &= E_0 \cos \alpha \exp(i(\omega t - kn_c z)), \\ E_\eta &= E_0 \sin \alpha \exp(i(\omega t - kn_o z)), \end{aligned} \quad (5)$$

i.e., there is an intercomponent phase shift proportional to the path traveled. The phase difference (incursion) after passing through the plate is expressed as

$$\Delta\varphi = 2\pi(n_e - n_o) \frac{d}{\lambda}, \quad (6)$$

where  $d$  is the thickness of the phase plate, and  $\lambda$  is the wavelength of light in a vacuum. Thus, an elliptically polarized wave is formed in the output plane of the plate [34]. The value of  $\Delta\varphi$ , according to (6), depends on the plate thickness, the wavelength, and the plate material.

Let us consider special cases:

(1)  $\Delta\varphi = 2\pi$  (a plate of one wavelength,  $\lambda$ ). As a result of summing two waves, a linearly polarized wave is formed at the output with an oscillation direction that coincides with that of the incident light wave.

(2)  $\Delta\varphi = \pi$  (a half-wave plate,  $\lambda/2$ ). At the output of the plate, a linearly polarized wave is also formed. The direction of oscillations of the electric field  $\mathbf{E}'$  in this case has a turn relative to the electric field vector  $\mathbf{E}$  of the incident wave by an angle of  $2\alpha$  or  $180^\circ - 2\alpha$ . Notably, the polarization plane will rotate by  $90^\circ$  at  $\alpha = 45^\circ$ .

(3)  $\Delta\varphi = \pi/2$  (quarter-wave plate,  $\lambda/4$ ). When two mutually perpendicular oscillations are summed, an ellipse with the major axes  $\xi$  and  $\eta$  is formed. In the particular case of

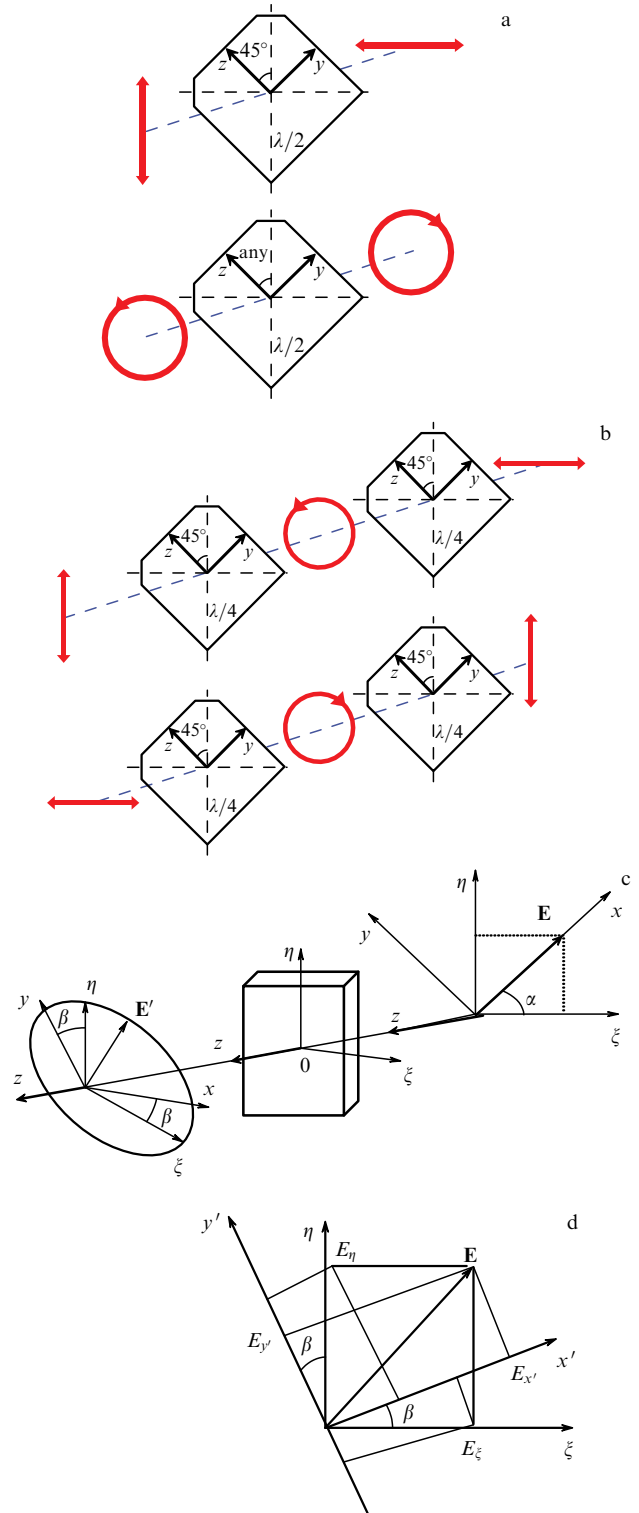


**Figure 6.** Widely used special cases of (a) half-wave and (b) quarter-wave plates. (c) General case of propagation of linearly polarized light through a waveplate. (d) Transition between coordinate systems of principal directions of waveplate to coordinate system of principal directions of analyzer.

$E_\xi = E_\eta$ , the transmitted light wave will be circularly polarized.

In all three of these cases, a monochromatic wave is obviously meant. If the monochromaticity condition is not met, polarization ellipses that differ from each other will arise at the output for different spectral components. The last two

cases, 2 and 3, are widely used in THz polarimetry (Figs 6a and 6b). To rotate the polarization plane of linearly polarized light by  $90^\circ$  or to change the direction of circular polarization, it is necessary to position the half-wave plate at a  $45^\circ$  angle of its optical axis to the plane of polarization of the incident light. Similarly, to convert linearly polarized light into circularly polarized and vice versa, a quarter-wave plate must be placed in a similar manner.

Polarimetry of elliptically polarized light involves finding the axes  $\xi$  and  $\eta$  and determining the direction of rotation of the vector  $\mathbf{E}$ . For example, if we consider a quartz phase plate ( $n_e > n_o$ ), the extraordinary wave, polarized along the  $\xi$  axis, has a lower propagation velocity in the medium. Therefore, at the output, the vector  $\mathbf{E}$  rotates clockwise when viewed along  $z$  (Fig. 6a). The parameters of the axes  $\xi$  and  $\eta$  can be determined using a simple scheme (with an analyzer medium), by measuring the maximum and minimum intensities of the transmitted light wave when the analyzer is rotated. Having rotated by an angle  $\beta$ , we switch to the coordinate system of the principal directions of the analyzer (Fig. 6d) from the coordinate system of the principal directions of the phase plate. One can see from Fig. 6d that the components  $E_{x'}$  and  $E_{y'}$  of the vector  $\mathbf{E}'$  in the axes  $x'$ ,  $y'$  are related to the components  $E_\xi$  and  $E_\eta$  using the expressions

$$\begin{aligned} E_{x'} &= E_\xi \cos \beta + E_\eta \sin \beta, \\ E_{y'} &= E_\xi \sin \beta + E_\eta \cos \beta. \end{aligned} \quad (7)$$

Let us direct the analyzer transmission axis along the  $x'$  direction. In this case, the transmitted wave intensity  $I \sim |E_{x'}|^2 = E_{x'} E_{x'}^*$ . Taking into account (5) and (6), we obtain

$$\begin{aligned} I &\sim E_0^2 (\cos^2 \alpha \cos^2 \beta + \sin^2 \alpha \sin^2 \beta + 2 \sin \alpha \sin \beta \\ &\quad \times \cos \alpha \cos \beta \cos \Delta\varphi). \end{aligned}$$

This expression describes two-beam interference at the analyzer output and depends on  $\Delta\varphi$  and interfering beam intensities  $I_1$  and  $I_2$ :

$$I = I_1 + I_2 + 2\sqrt{I_1 I_2} \cos \Delta\varphi. \quad (8)$$

These intensities depend on the angles of the mutual positions of the analyzer, phase plate, and polarizer:  $I_1 = I_0 \cos^2 \alpha \cos^2 \beta$  and  $I_2 = I_0 \sin^2 \alpha \sin^2 \beta$ . Obviously, removing the phase plate (in this case, the phase incursion  $\Delta\varphi = 0$ ) will lead to Malus's law,  $I = I_0 \cos^2 \delta$ , where  $\delta$  is the difference  $\alpha - \beta$ , equal to the angle between the transmission axes of the analyzer and the polarizer. The situation when only the angle  $\beta$  changes, with the angle  $\alpha$  being constant, is the rotation of the analyzer with the stationary plate and polarizer. If the value of  $\beta$  satisfies the condition

$$\tan(2\beta) = \tan(2\alpha) \cos(\Delta\varphi), \quad (9)$$

then the value of the light intensity at the analyzer output will acquire a minimum or maximum value and

$$\frac{I_{\max} - I_{\min}}{I_{\max} + I_{\min}} = (1 - \sin^2(2\alpha) \sin^2(\Delta\varphi))^{1/2}. \quad (10)$$

Expression (10) relates the values of  $\alpha$  and  $\Delta\varphi$  with the values of  $I_{\max}$  and  $I_{\min}$  for the semi-axes of the polarization ellipse, and expression (9) allows the orientation of the semi-axes to be determined.

As was indicated above, to convert THz radiation polarization, waveplates (WPs) are made of crystalline quartz due to its transparency in the THz region; for the same reason, sapphire can also be used. Quartz waveplates make it possible to convert polarization of THz radiation in the range from 30 to 1000  $\mu\text{m}$ . For industrially manufactured WPs, an orientation tolerance of  $\pm 10$  arc min, a thickness tolerance of  $\pm 0.25 \mu\text{m}$ , and a surface quality of  $-60/40$  scr/dig are usually allowed in optical production.

It should be noted separately that the use of a segmented plate consisting of several half-wave plates oriented in a certain way relative to each other allows radially and azimuthally polarized radiation to be obtained from linearly polarized light. Let us dwell on this issue in more detail. Most studies in the field of polarization optics consider spatially homogeneous states of polarization, i.e., linear, elliptical, and circular. In these cases, spatially homogeneous states of polarization do not depend on the spatial arrangement of the cross section of the light beam. At the same time, there are a number of applications of light beams with spatially different spatially homogeneous states of polarization. A specific example is an application related to laser radiation with cylindrical polarization symmetry, so-called beams with a cylindrical vector (CV).

In a number of THz optics problems, it is often necessary to form a focused radiation spot of minimal area. When focusing a light beam, the shape of the phase front determines the shape and size of the focal spot. Due to polarization effects, the energy distribution density in the spot, for example for linearly polarized light, does not have rotational symmetry [35]. To obtain a circular focal spot, the polarization distribution in the incident beam must have rotational symmetry, for example, radial or azimuthal. In this case, the field is linearly polarized at each point of the beam cross section, but the polarization axis changes from point to point. Dorn et al. [36] showed that a distribution in the form of a radially polarized ring (so-called ring mode) allows one to form the smallest possible focal spot. Dorn et al. [37] also demonstrated that, for tightly focused beams, a longitudinal electric field is generated along the optical axis for a radially polarized field, and a longitudinal magnetic field is correspondingly generated for an azimuthally polarized field. Such longitudinal field components are also of significant interest for many optical applications. A collimated radially polarized annular mode can be described as a coherent superposition of two orthogonally linearly polarized first-order Gauss–Hermite modes or as a superposition of the corresponding left- and right-hand modes with circularly polarized Gauss–Laguerre modes. In both cases, the modes must be in phase.

Let us consider in more detail the formation of CV beams. These beams are solutions to Maxwell's equations that have axial symmetry of both amplitude and phase [38, 39]. Wave modes with radial or azimuthal polarization are well known in waveguide theory. However, their analogues in conventional, nonwaveguide media are less well known. For such media, a typical solution with a harmonic time dependence is obtained by solving the scalar Helmholtz equation:

$$(\nabla^2 + k^2) E = 0, \quad (11)$$

where  $k = 2\pi/\lambda$  is the wave number. For the solution describing a paraxial beam in Cartesian coordinates, the general solution for the electric field has the form

$$E(x, y, z, t) = u(x, y, z) \exp(i(kz - \omega t)). \quad (12)$$

Using a slowly varying envelope approximation,

$$\frac{\partial^2 u}{\partial z^2} \ll k^2 u, \quad \frac{\partial^2 u}{\partial z^2} \ll k \frac{\partial u}{\partial z}, \quad (13)$$

yields a solution for the Hermite–Gaussian modes  $\text{HG}_{mm}$  by separation of variables. Mathematically, this solution in the radially symmetric case can be reduced to the form describing a fundamental Gaussian beam:

$$u(r, z) = E_0 \frac{w_0}{w(z)} \exp \left[ -i \left( \varphi(z) - \frac{kr^2}{2q(z)} \right) \right], \quad (14)$$

where  $\varphi(z) = \arctan(z/z_0)$  is the Gouy phase shift;  $E_0$  is the constant amplitude of the electric field;  $w(z)$  is the beam size depending on the coordinate;  $w_0$  is the beam size at the waist; and  $q(z) = z - iz_0$  is a complex parameter describing the beam, with  $z_0 = \pi w_0^2/\lambda$  being the Rayleigh parameter. In this case, Eqn (12) can be written in the form

$$E(r, \phi, z, t) = u(r, \phi, z) \exp(i(kz - \omega t)). \quad (15)$$

Substituting (15) into the scalar Helmholtz equation (11) with (13) taken into account leads to an equation in cylindrical coordinates

$$\frac{1}{r} \frac{\partial}{\partial r} \left( r \frac{\partial u}{\partial r} \right) + \frac{1}{r^2} \frac{\partial^2 u}{\partial \phi^2} + 2ik \frac{\partial u}{\partial z} = 0. \quad (16)$$

From Eqn (16), by separating the variables  $r$  and  $\phi$ , one can obtain two types of solutions, which are Laguerre–Gaussian modes  $\text{LG}_{pl}$  in the first case, and a solution that has rotational symmetry, i.e., does not depend on the azimuthal angle  $\phi$  (see [40]), a so-called scalar solution for the Bessel–Gaussian beam:

$$\begin{aligned} u(r, \phi, z) &= E_0 \left( \sqrt{2} \frac{r}{\omega} \right)^l L_p^l \left( 2 \frac{r^2}{\omega^2} \right) \frac{w_0}{w(z)} \\ &\quad \times \exp \left[ -i \left( \varphi_{pl}(z) - \frac{kr^2}{2q(z)} - l\phi \right) \right], \\ u(r, z) &= E_0 \frac{w_0}{w(z)} \exp \left[ -i \left( \varphi_{pl}(z) - \frac{kr^2}{2q(z)} \right) \right] \\ &\quad \times J_0 \left( \frac{\beta r}{1 + i(z/z_0)} \right) \exp \left( -\frac{\beta^2(z/2k)}{1 + i(z/z_0)} \right). \end{aligned} \quad (17)$$

Here,  $L_p^l(x)$  are the Laguerre polynomials,  $\varphi(z)$  and  $\varphi_{pl}(z) = (2p + l + 1) \arctan(z/z_0)$  are the Gouy phase shifts for the two cases,  $\beta$  is the scaling parameter, and  $J_0(x)$  is the zero-order Bessel function of the first kind. At  $l = p = 0$ , the first solution reduces to the form characteristic of a fundamental Gaussian beam. The above-obtained solutions (Hermite–Gaussian, Laguerre–Gaussian, and Bessel–Gaussian) are paraxial solutions of the Helmholtz scalar equation (11) for a light beam, corresponding to spatially homogeneous polarization states, or scalar beams. For these beams, there are spatially homogeneous states of polarization, i.e., the form of oscillation of the electric field vector does not depend on the position of the observation point in the beam cross section. However, if we consider the full vector wave equation for the electric field [38],

$$(\nabla \times \nabla \times \mathbf{E}) - k^2 \mathbf{E} = 0, \quad (18)$$

expression (5) is reduced to the form

$$\mathbf{E}(r, z) = U(r, z) \exp(i(kz - \omega t)) \mathbf{e}_\phi, \quad (19)$$

where the exponent includes a unit vector depending on the azimuthal angle, and  $U$  satisfies the modified equation (16), which has the form

$$\frac{1}{r} \frac{\partial}{\partial r} \left( r \frac{\partial U}{\partial r} \right) - \frac{U}{r^2} + 2ik \frac{\partial U}{\partial z} = 0. \quad (20)$$

The solution to this equation has a form similar to (17), but already taking into account the radial symmetry of polarization:

$$\begin{aligned} \mathbf{E}(r, z) &= -E_0 J_1 \left( \frac{\beta r}{1 + i(z/z_0)} \right) \exp \left( -\frac{\beta^2(z/2k)}{1 + i(z/z_0)} \right) \\ &\quad \times u(r, z) \exp(i(kz - \omega t)) \mathbf{e}_\phi, \\ U(r, z) &= E_0 J_1 \left( \frac{\beta r}{1 + i(z/z_0)} \right) \exp \left( -\frac{\beta^2(z/2k)}{1 + i(z/z_0)} \right) u(r, z), \end{aligned} \quad (21)$$

where  $J_1(x)$  is the first-order Bessel function of the first kind. In this case, there is a similar solution (19) for the transverse magnetic field vector, which also includes a unit vector depending on the azimuthal angle. This solution corresponds to the azimuthal distribution, i.e., the presence of radial polarization of the magnetic field, which in turn leads to the presence of a radial distribution of the electric field in the plane orthogonal to the magnetic field vector. In this way, CV beams are described. They can be radially or azimuthally polarized, i.e., their electric field vector has a radial or azimuthal distribution.

In a number of applications for CV beams, other simplified distributions can be used instead of Bessel–Gaussian vector solutions [41]. For example, at small  $\beta$  for the vector solution for a Bessel–Gaussian beam, one can write

$$\mathbf{E}(r, z) = A r \exp \left( -\frac{r^2}{w^2} \right) \mathbf{e}_i, \quad \text{where } i = r, \phi. \quad (22)$$

It can be shown [42] that CV beams can be represented as a superposition of orthogonally polarized Hermite–Gaussian modes  $\text{HG}_{01}$  and  $\text{HG}_{10}$ :

$$\begin{aligned} \mathbf{E}_r &= \text{HG}_{10} \mathbf{e}_x + \text{HG}_{01} \mathbf{e}_y, \\ \mathbf{E}_\phi &= \text{HG}_{01} \mathbf{e}_x + \text{HG}_{10} \mathbf{e}_y, \end{aligned} \quad (23)$$

where  $\mathbf{E}_r$  and  $\mathbf{E}_\phi$  correspond to radial and azimuthal polarization, respectively.

There are several methods for generating CV beams. The so-called passive generation involves the use of nematic liquid crystals or segmented waveplates to convert linearly or circularly polarized beams. The second technique has become widespread in THz polarimetry. In this case, a waveplate is used, consisting of separate segments, in each of which the optical axis has its own direction. For example, in the case of a linearly polarized beam at the input, a set of glued (4, 8, etc., segments) half-wave phase plates can be used to convert it into a CV beam [43, 44]. For incident circularly polarized light, segmental gluing of quarter-wave phase plates with a radial arrangement of optical axes is used, which makes

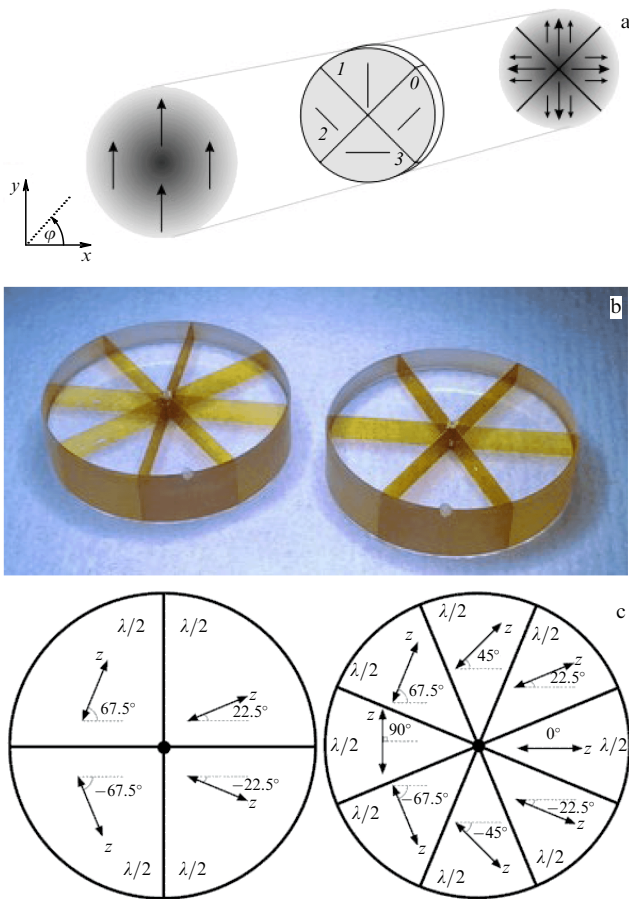


**Figure 7.** (a) Example explaining operation of a segmented half-wave plate: polarization reversal in a separate section of original linearly polarized beam by each of four segments, forming a radial polarization distribution in resulting CV beam (borrowed from [41]). (b) Example and (c) diagram of a segmented waveplate for converting radial into circular polarization (borrowed from [45]).

it possible to obtain a CV beam with a cylindrical polarization distribution. Thus, a certain part of the original beam is incident on each of the plate segments, which, after passing the segment, acquires its own polarization direction (see the example for a four-segment WP in Fig. 7a, where in each region the polarization of the corresponding part of the linearly polarized incident beam rotates by 90°). Thus, the final polarization distribution in the beam that has passed the segmented WP will be spatially distributed, forming a CV beam. However, it is clear that, due to the limited number of half-wave segments and, as a consequence, the discreteness of the optical axis directions, this type of device does not provide accurate spatial alignment of polarization. In the case of a fundamental Gaussian beam with a parameter  $\omega_0$  at the input, the distribution of the electric field formed at the output depends on the total number of segments  $m$  and can be described by transformed formula (22):

$$\mathbf{E}(r, \varphi) = A_0 \sqrt{\frac{2}{\pi \omega_0^2}} \left( \cos \frac{2\pi n}{m}, \sin \frac{2\pi n}{m} \right) \exp\left(-\frac{r^2}{w^2}\right),$$

where  $n = 0, \dots, m - 1$ . (24)

The degree of overlap (superposition) of the transmitted field  $E(r, \varphi)$  (see Eqn (24)) with the ideal fully radially polarized

annular mode  $E_R(r, \varphi)$  with the beam parameter  $\omega_R$  can be described by the formula

$$C(m, \omega_R, \omega_0) = m \int_0^\infty \int_{-\pi/m}^{\pi/m} d\varphi dr r \mathbf{E}(r, \varphi = 0, \omega_0) \mathbf{E}_R(r, \varphi, \omega_R),$$

which can be transformed into

$$C(m, \omega_R, \omega_0) = A_0^2 \sqrt{\frac{2}{\pi}} \frac{\omega_0^2 \omega_R}{(\omega_0^2 + \omega_R^2)^{3/2}} m \sin \frac{\pi}{m}. \quad (25)$$

Higher-order transverse modes, which are also present in the transmitted field, can be suppressed by subsequent focusing of the beam in a Fabry–Perot interferometer (FPI), which operates as a mode filter and is also used in THz photonics. When using a four-segment WP, the transmitted field  $E(r, \varphi)$  has a degree of overlap of 75% with the ideal annular mode  $E_R(r, \varphi)$ . This value can be increased to 87% if the number of segments is increased to eight, or to 92% if the number of segments tends to infinity (the value of 100% cannot be achieved due to diffraction losses). If a half-wave plate is additionally placed before the segmented WP, polarization of the incident beam can be rotated, which will ensure switching of the distribution of radial and azimuthal polarizations at the output of the optical system. An example and diagram of an industrially manufactured segmented WP, which allows radial polarization to be converted from circular polarization, are shown in Figs 7b and 7c (borrowed from [45]). Each segment of such a plate converts the polarization of the corresponding section of the original beam in such a way that the overall behavior of the polarization vector exhibits radial symmetry.

When this plate is rotated 45°, radiation at the output will have azimuthal polarization, and when the plate is rotated 90°, it will have radial polarization of the opposite direction. To obtain polarized radiation, the polarization vector of which coincides with the propagation direction of radiation, the segmented plate can be used in combination with a collecting lens.

### 2.4 Other polarization converters

All components based on crystalline quartz, including well-known Glan–Taylor, Glan–Foucault, Wollaston, and Nicol prisms, are suitable for converting THz radiation due to its transparency in the THz region. These elements serve to isolate linearly polarized light by spatially separating ordinary and extraordinary beams. They were developed in the 19th and first half of the 20th centuries.

The Wollaston prism is an optical device consisting of two orthogonal triangular prisms made of a uniaxial birefringent material. These prisms are fastened together at the boundary of their bases (traditionally using Canadian balsam or an optical contact) so that their optical axes are mutually perpendicular. The emerging ordinary and extraordinary beams diverge from the Wollaston prism with spatial separation due to differences in refractive indices, with the divergence angle being determined by the wedge angle of the prisms and the wavelength of the light (Fig. 8a). Commercial Wollaston prisms for THz radiation are produced by Thorlabs [47].

Other devices that provide spatial distribution of polarized ordinary and extraordinary beams are Glan–Foucault and Glan–Taylor prisms consisting of two connected rectangular prisms made of birefringent materials separated by an

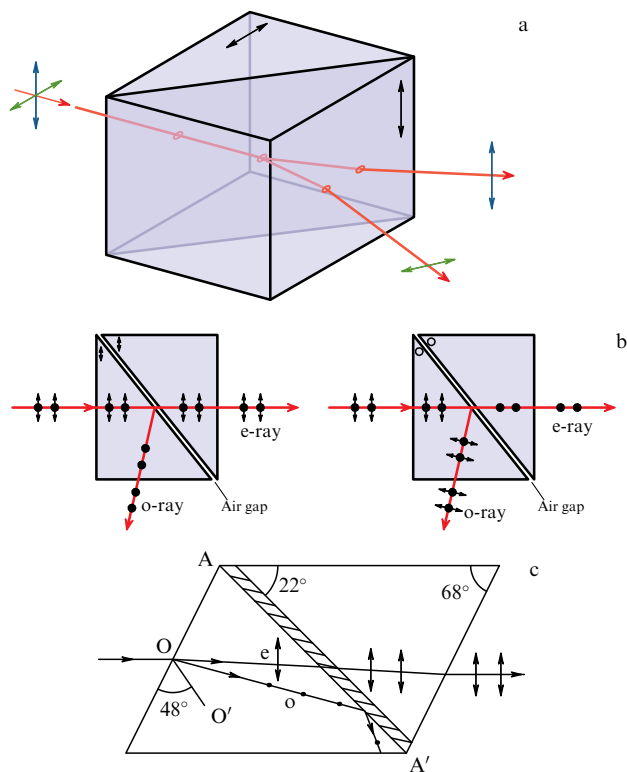


**Figure 8.** (a) Wollaston prism (borrowed from [46]). (b) Glan–Taylor (left) and Glan–Foucault (right) prisms (borrowed from [51]). (c) Nicol prism (borrowed from [48]).

air gap; their structural difference lies in the fact that, in the first case, the optical axis is orthogonal to the plane of the triangular face of the prism, while, in the second case, the optical axis is in the profile plane. The Glan–Taylor variant is one of the most commonly used prisms today and is designed to convert arbitrarily polarized radiation into linearly polarized radiation [49]. The design was proposed by Archard and Taylor in 1948 [50]. Schematic representations of Glan–Foucault and Glan–Taylor prisms are shown in Fig. 8b. Total internal reflection of s-polarized light from the air gap for the Glan–Taylor prism ensures that only p-polarized light is transmitted by the device. Conversely, in the Glan–Foucault prism [52], only s-polarized light is transmitted by the device. Since the angle of incidence on the gap can be close enough to the Brewster angle, unwanted reflection of p- and s-polarized light for the Glan–Taylor and Glan–Foucault prisms, respectively, is reduced. The sides of the crystal can be polished to allow the reflected beam to pass through, or blackened to absorb it. The latter reduces the unwanted Fresnel reflection of the deflected beam.

One more traditional birefringent device is the Nicol prism (Fig. 8c), which is usually used for visible light. However, if it is made of crystalline quartz rather than calcite, it can be used in the THz region. The Nicol prism consists of two identical triangular prisms made of Iceland spar, glued with a thin layer of Canadian balsam. Traditionally, prisms are made so that the end face is beveled at an angle of 68° relative to the direction of the transmitted light, and the glued sides form a right angle with the end faces. In this case, the optical axis of the crystal (AB) is at an angle of 64° with the direction of light. The aperture of full polarization of the prism is 29°. A special feature of the prism is a change in the

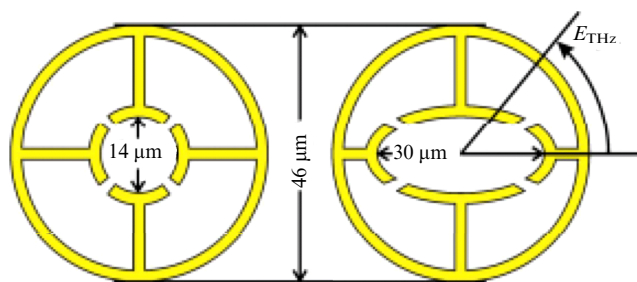


**Figure 9.** Geometry of circular (left, polarization-insensitive) and elliptical (right, polarization-sensitive) ring resonators with their size. Measurement of angle between incident THz electric field vector  $E$  relative to major axis of ellipse (right) is shown (borrowed from [59]).

direction of the output beam during rotation of the prism, resulting from refraction of the beveled end faces of the prism.

Polarization converters based on metamaterials (MMs) should be mentioned separately. In general, THz metamaterials are two-dimensional periodic structures in the form of slits of a certain shape on a metal plate or, on the contrary, metal two-dimensional objects applied to a film transparent in the THz range (frequency selective surfaces [53–55]). These structures can transmit or reflect incident radiation of certain frequencies. These objects also serve to convert the phase of incident THz radiation, can play the role of bandpass or cutoff filters, etc. There are many papers and a number of reviews devoted to MMs (see, for example, [56]). The most common are split ring resonators (SRRs) [57, 58]. Terahertz metamaterials, with a certain configuration, can serve as THz polarization converters. For example, in their well-known paper, Peralta et al. [59] describe metamaterials that are a series of two-dimensional objects of an elliptical configuration (Fig. 9).

The same paper shows that two parallel plates of this configuration can play the role of a quarter-wave phase plate at a frequency of 1.06 THz. Several papers on MM-based WPs are known (see, for example, [60–62]).

### 3. Polarizer-based devices

#### 3.1 Achromatic waveplates

Conventional waveplates described in Section 2.3 are made of birefringent materials and exhibit phase retardation properties for incident radiation. This retardation depends on the thickness of the plates, limiting their application to certain frequencies. However, waveplates with a wide spectral range are required for application in THz-TDS. A conventional waveplate is designed for a specific wavelength. There is a concept of an achromatic waveplate, i.e., a plate designed for a certain wavelength range. Masson and Gallot [63] published one of the first research papers where they discussed a THz achromatic waveplate (AWP) made of monochromatic waveplates stacked together at the visible optical contact. Achromatic WPs provide phase retardation in a wide range of wavelengths. Several unconventional approaches to the design of THz AWTs have been demonstrated. Zhang et al. [64] considered polymer composites with birefringence. Cong et al. [65] described an AWP based on metamaterials, and Kawada et al. [66] considered an achromatic prism-type waveplate utilizing phase retardation by total internal reflection. The authors of Refs [67, 68] describe stacks of

parallel metal plates providing specific polarization rotation in the THz range. Two-dimensional metal gratings consisted of offset paired metal layers of complementary chiral structures with fourth-order symmetry. It was shown that the polarization rotation does not depend on the polarization direction of isotropic incident radiation. In this case, the rotation of the plane of polarization was calculated by calculating the components of the Jones matrices  $\hat{T}$ , which relate the components of the electric vector of the incident  $\mathbf{E}_{\text{sam}}$  and transmitted  $\mathbf{E}_{\text{tr}}$  waves by the expression  $\mathbf{E}_{\text{tr}} = \hat{T} \mathbf{E}_{\text{sam}}$ , where  $\hat{T}$  has the form

$$\hat{T} = \begin{pmatrix} \tilde{t}_1 & \tilde{t}_2 \\ -\tilde{t}_2 & \tilde{t}_1 \end{pmatrix}, \quad (26)$$

and solving the Newton–Raphson equation relative to the diagonal component of the Jones matrix

$$\tilde{t}_1 = \frac{2}{1 + \tilde{n}} \frac{2\tilde{n}}{1 + \tilde{n}} \exp\left(i\omega \frac{(\tilde{n} - 1)L}{c}\right), \quad (27)$$

where the diagonal component of the permittivity tensor is related to the complex refractive index by the expression  $\tilde{\epsilon} = \epsilon_0 \tilde{n}^2$ , and  $L$  is the thickness of the entire stack. The Jones matrix method will be described in more detail below.

There are known papers that describe the use of liquid crystals (LCs) (see [69]) as AWP. In particular, the indicated paper describes the calculation and fabrication of an LC plate in which transmission is related to the applied voltage by the expression

$$\delta(V) = \int_0^d \frac{2\pi f}{c} \partial n_{\text{eff}}(V, z) dz, \quad (28)$$

$$\partial n_{\text{eff}} = \left( \frac{\cos^2 \theta}{n_o^2} + \frac{\sin^2 \theta}{n_e^2} \right)^{-1/2} - n_o.$$

Here,  $f$  is the frequency of THz radiation,  $\partial n_{\text{eff}}(V, z)$  is the change in the effective birefringence for the LC at position  $z$  along the direction of THz radiation propagation, and  $\theta$  is the angle of deviation of LC molecules from the initial one under the action of voltage  $V$ . The same authors showed that, in the THz range, 4'-p-pentyl-4-cyanobiphenyl (5CB), a commonly used nematic liquid crystal, has fairly high birefringence ( $\sim 0.2$ ) and a small attenuation coefficient at frequencies of about 1 THz (see [70, 71]). They also demonstrated the first tunable THz phase shifter at room temperature, implementing a  $360^\circ$  phase shift at a frequency of 1 THz [72–74], which is a magnetically controlled cell of a nematic liquid crystal, providing a change in birefringence.

Known also are an exotic case of an AWP based on a silicon grating [75] and a variable polarization compensator based on two interlocking V-shaped silicon gratings at 100 GHz [76, 77].

However, the above-described waveplates are either difficult to manufacture or do not demonstrate sufficiently good characteristics due to optical loss. In addition, the AWP of the above-mentioned types operated in an insufficiently wide spectral range. A number of papers [78–83] described AWP consisting of quartz or sapphire plates with optical contact and optical birefringence axes lying in the plane of the plates. Such waveplates are much easier to manufacture, and, most importantly, they operate in a significantly wider frequency range.

A number of papers, including those mentioned above, are devoted to methods of calculating AWP made of quartz

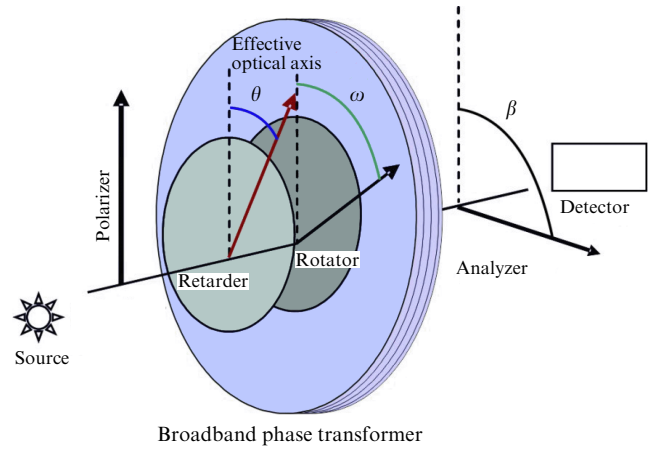


**Figure 10.** Schematic of a system of plane-parallel birefringent media with birefringence axes lying in a plane (borrowed from [83]).

and sapphire. For cases where a high resolution of the system is required compared to the half-width of the interference maxima, it is necessary to introduce corrections. In this regard, a modification of the methods for calculating real, practically significant AWP was developed, taking into account the interference effect; this method served as a basis for the manufacture of AWP [84]. Kaveev et al. [83] considered in detail a calculation and simulation method and also described the manufacture of a broadband THz polarization converter of the specified type, which is an AWP consisting of a stack of parallel planar birefringent plates, transparent in the THz wavelength range. It was shown that it is possible to design AWP for different wavelength ranges by stacking together monochromatic plates in AWP at different angles and using different plate thicknesses. It is also possible to fabricate AWP for different phase delays (in particular,  $\lambda/4$  and  $\lambda/2$ ).

Pancharatnam [79] published one of the pioneering papers on AWP calculation. However, a more compact and convenient calculation method is based on the Jones matrix formalism. According to the Jones formalism [85, 86], a system of any finite set of wave plates is optically equivalent to a system containing only two elements—so-called retarder and rotator (Fig. 10).

A retarder provides the required phase shift (for example,  $\pi$  or  $\pi/2$ ). A rotator rotates the plane of polarization by an angle  $\omega$ . Depending on the value of the angle  $\omega$ , there are two types of polarization converters: (i)  $\omega$  is close to zero in the operating range of wavelengths. In this case, this is a conventional AWP and its operating principle is the same as that of a monochromatic waveplate. When delayed by  $\theta$ , the plane of polarization of the radiation passed through the AWP is located at an angle of  $2\theta$  to the polarizer axis, where  $\theta$  is the angle of the effective optical axis of the AWP; and (ii)  $\omega$  depends on the wavelength. In this case, the object is not an ordinary AWP, but is essentially a broadband polarization converter (broadband waveplate, BWP), which is a special case of the AWP. For example, when converting circular into linear polarization, the polarization plane of radiation transmitted through the converter is oriented at an angle of  $\beta = \omega \pm 45^\circ$  to the polarizer axis. In the case of rotation of the linear polarization plane,  $\beta = \omega + 2\theta$ . Kaveev et al. [83] calculated AWP and BWP for the cases of  $\lambda/4$  and  $\lambda/2$  in different THz wavelength ranges.

Taking into account interference effects, Savini et al. [78] calculated BWPs using a modified  $4 \times 4$  Jones matrix written for each individual plate in the stack:

$$\hat{Q} = \begin{pmatrix} \cos(k_e d) & i n_e \sin(k_e d) & 0 & 0 \\ i \frac{1}{n_e} \sin(k_e d) & \cos(k_e d) & 0 & 0 \\ 0 & 0 & \cos(k_o d) & i n_o \sin(k_o d) \\ 0 & 0 & i \frac{1}{n_o} \sin(k_o d) & \cos(k_o d) \end{pmatrix}, \quad (29)$$

where  $k_e = 2\pi n_e/\lambda$  and  $k_o = 2\pi n_o/\lambda$ ,  $d$  is the thickness of a given quartz plate, and  $n_e$  and  $n_o$  are the refractive indices of the extraordinary and ordinary rays, respectively. The final Jones matrix of the system of  $N$  plane-parallel plates is the product of  $N$  matrices of type (29) for each plate:

$$\hat{M} = \prod_{j=1}^N (\hat{F}_j \hat{Q}_j \hat{F}_j^{-1}). \quad (30)$$

Here,

$$\hat{F} = \begin{pmatrix} \cos \varphi & 0 & -\sin \varphi & 0 \\ 0 & \cos \varphi & 0 & -\sin \varphi \\ \sin \varphi & 0 & \cos \varphi & 0 \\ 0 & \sin \varphi & 0 & \cos \varphi \end{pmatrix} \quad (31)$$

is the  $4 \times 4$  rotation matrix describing the angular position of the  $i$ th plate relative to the plane of polarization of incident radiation. The matrix  $\hat{M}$  relates the vectors of the electric and magnetic fields of the waves incident, transmitted, and reflected from the system. The matrix that determines the polarization of the incident wave from the known polarization of the transmitted wave has the form

$$\hat{P} = \begin{pmatrix} \frac{M_{11} + M_{12} + M_{21} + M_{22}}{2} & \frac{M_{13} + M_{14} + M_{23} + M_{24}}{2} \\ \frac{M_{31} + M_{32} + M_{41} + M_{42}}{2} & \frac{M_{33} + M_{34} + M_{43} + M_{44}}{2} \end{pmatrix}. \quad (32)$$

The polarization of the transmitted wave can be calculated from the known polarization of the incident wave using the matrix  $\hat{P}^{-1}$ . This matrix is an analogue of the simple [86] Jones matrix  $2 \times 2$ . Taking into account the interference effect in a system of waveplates shows that the system behaves differently when linear polarization is converted to circular and vice versa.

The described system behaves like an AWP with an unchanging angular position of the effective optical axis (EOA) along the polarizer axis  $x$  in the wavelength range in which the off-diagonal elements of the simple Jones matrix  $2 \times 2$

$$\hat{J} = \prod_{i=1}^N \hat{J}_i, \quad \hat{J}_i = \begin{pmatrix} \cos\left(\frac{\delta_i}{2}\right) + i \cos(2\varphi_i) \sin\left(\frac{\delta_i}{2}\right) & i \sin(2\varphi_i) \sin\left(\frac{\delta_i}{2}\right) \\ i \sin(2\varphi_i) \sin\left(\frac{\delta_i}{2}\right) & \cos\left(\frac{\delta_i}{2}\right) - i \cos(2\varphi_i) \sin\left(\frac{\delta_i}{2}\right) \end{pmatrix} \quad (33)$$

are close to zero, the moduli of the diagonal elements are close to unity, and the phase difference of the diagonal elements is equal to a given retardation (here,  $\delta_i = 2\pi(n_e - n_o)d_i/\lambda$ , and  $\varphi_i$  is the EOA angle of the plate relative to the polarizer axis).

A set of  $(\delta_i, \varphi_i)$  values corresponding to the  $i$ th waveplate is found using the so-called simulated annealing algorithm developed by S. Kirkpatrick [80, 87, 88]. Depending on the minimization parameters when searching for their values, two above-mentioned situations are possible:  $\omega \approx \text{const}$  (in the particular case 0) and  $\omega \neq \text{const}$ . In essence, the angle  $\omega$  is the angle of rotation of the effective rotator.

It is possible to calculate the wavelength dependence of the degree of polarization, i.e., the fraction of the intensity of linearly polarized light in the total intensity. For the case of ideal circular polarization, this value is zero; when converting linear (along the  $x$ -axis) into circular polarization, the value is calculated using the formula

$$I = \frac{|E_2 \bar{E}_2 - E_1 \bar{E}_1|}{E_2 \bar{E}_2 + E_1 \bar{E}_1}, \quad (34)$$

where

$$E_1 = P_{11}^{-1} \cos(\eta) + P_{21}^{-1} \sin(\eta), \quad (35)$$

$$E_2 = P_{21}^{-1} \cos(\eta) - P_{11}^{-1} \sin(\eta),$$

$$\eta = 0.5 \arctan\left(\frac{P_{11}^{-1} \bar{P}_{21}^{-1} + P_{21}^{-1} \bar{P}_{11}^{-1}}{P_{11}^{-1} \bar{P}_{11}^{-1} + P_{21}^{-1} \bar{P}_{21}^{-1}}\right). \quad (36)$$

An example of such a dependence for the AWP is shown in Fig. 11a. This AWP has a total thickness of 7.462 mm (the thicknesses of the plates in the stack are 0.745, 0.790, 0.797, 1.533, 1.597, and 2.000 mm), a clear aperture of 25 mm or more, and a conversion error of  $\pm 15\%$ .

The EOA angle for a quarter-wave polarization converter is related to the components of the Jones matrix by the expression

$$\theta = 0.5 \times \left| \arctan\left(\frac{\text{Im}(P_{12}^{-1} \exp(-iv)) \text{Re}(P_{11}^{-1} \exp(-iv)) + \text{Re}(P_{12}^{-1} \exp(-iv)) \text{Im}(P_{11}^{-1} \exp(-iv))}{\text{Im}(P_{11}^{-1} \exp(-iv)) \text{Re}(P_{11}^{-1} \exp(-iv)) - \text{Re}(P_{12}^{-1} \exp(-iv)) \text{Im}(P_{12}^{-1} \exp(-iv))}\right) \right|, \quad (37)$$

where  $v_1 = 0.5 \arg(-P_{12}^{-1} P_{21}^{-1})$ ,  $v_2 = 0.5 \arg(-P_{11}^{-1} P_{22}^{-1})$  are the phases. The exponential factor in this expression arises because the analogue of the simple Jones matrix  $\hat{P}^{-1}$  does not have the same form as in formula (33). This is due, first to interference, and second, to the fact that it is multiplied by the total phase shift in the polarization converter. In order to approximately use the formulas for  $\delta$ ,  $\theta$ , and  $\omega$ , valid for the simple Jones matrix (33), it is necessary to multiply the matrix  $\hat{P}^{-1}$  by the term  $\exp(-jv)$ . In this case, it is necessary to check that the phase values calculated from the diagonal and off-diagonal elements of the matrix are close. Figure 11b shows an example of the dependence of the phase  $v$  on the wavelength for the range of 100–150  $\mu\text{m}$ , calculated for the same AWP. In this case, the graph is the same for  $v_1$  and  $v_2$ . The angle  $\omega$  can be found using the formula

$$\omega = \arctan\left(-\frac{\text{Re}(P_{12}^{-1} \exp(-iv))}{\text{Re}(P_{11}^{-1} \exp(-iv))}\right). \quad (38)$$

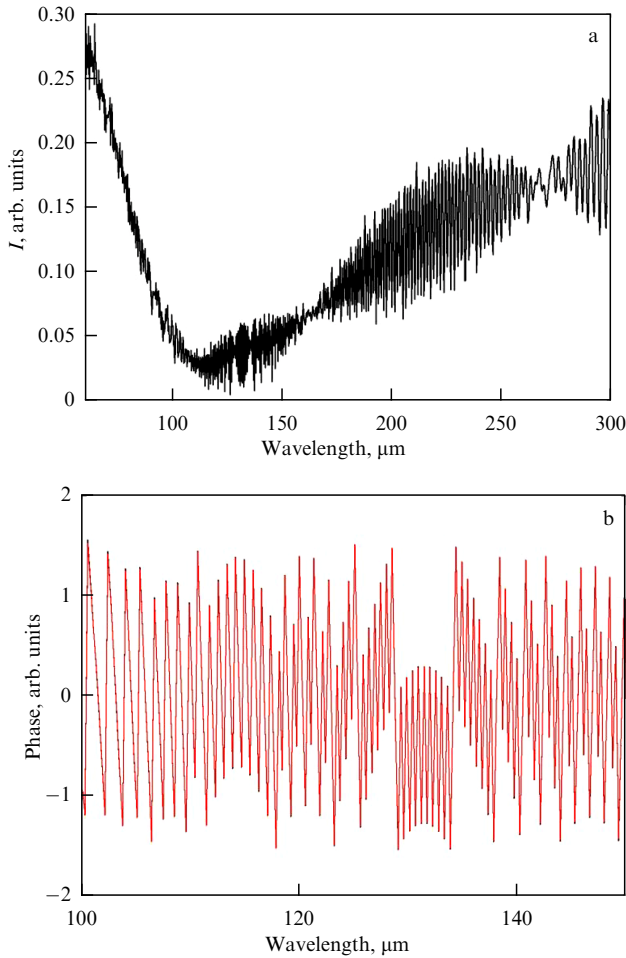


**Figure 11.** (a) Wavelength dependence of fraction of linearly polarized light intensity in total intensity for light with polarization converted into circular polarization by an AWP designed for an operating range of 60–300  $\mu\text{m}$ . (b) Wavelength dependence of phase in range of 100–150  $\mu\text{m}$  for same AWP. (Borrowed from [83].)

Finally, retardation of the system can be calculated as follows. For the matrix  $\hat{P}^{-1}$  with off-diagonal elements close to zero,

$$\delta = \arg(P_{22}^{-1}) - \arg(P_{11}^{-1}) \quad (39)$$

will hold true. In the general case, retardation can be calculated through the elements of the matrix  $\hat{P}^{-1}$ , and not all of its elements are used in the calculation. For example:

$$\delta = \arctan \left[ \left( \frac{(\text{Im}(P_{11}^{-1} \exp(-iv)))^2 + (\text{Im}(P_{12}^{-1} \exp(-iv)))^2}{(\text{Re}(P_{11}^{-1} \exp(-iv)))^2 + (\text{Re}(P_{12}^{-1} \exp(-iv)))^2} \right)^{0.5} \right]. \quad (40)$$

Thus, in the general case, a nonabsorbing achromatic polarization converter is characterized by three quantities:  $\delta$ ,  $\theta$ , and  $\omega$ . The last must be taken into account, for example, when converting circular polarization into linear polarization with a quarter-wave converter. The position of the polarization plane of the light transmitted by the converter will depend on  $\omega$ . The polarization of the light transmitted through the achromat will be at an angle of  $\omega \pm 45^\circ$  relative to the polarizer axis.

The use of matrix (29), in contrast to matrix (33), is justified when taking into account that interference in the system is necessary from a practical point of view, for example, when the width of the spectral band of radiation from the used source is less than the characteristic width of the interference maxima. The spectral bandwidth can be estimated by the wavelength using a simple formula:  $\Delta\lambda = \lambda^2 \Delta f / c$ , where  $\Delta f$  is the frequency bandwidth. Then, a comparison is made with the interference period obtained from the dependence of  $\delta(\lambda)$  for the same wavelength. If  $\Delta\lambda$  is greater than the interference period, then matrix (33) can usually be used for calculations.

Examples of the dependences of  $\delta(\lambda)$ ,  $\varphi(\lambda)$ , and  $\omega(\lambda)$  calculated for the cases of  $2 \times 2$  and  $4 \times 4$  Jones matrices (with  $\omega \approx \text{const}$  and  $\omega \neq \text{const}$ ) for a tunable AWP with a double-sided antireflection coating are shown in Fig. 12. One can see from the figure that the curves for different Jones matrices coincide, but the interference contribution, which is most significant for  $\varphi(\lambda)$  and  $\delta(\lambda)$ , manifests itself in the ‘noisiness’ of the dependences at the selected wavelengths. The significance of the contribution for  $\omega(\lambda)$  is less so. Note that without an antireflective coating, the dependence on interference will be significantly more pronounced. For AWP, the dependences of  $\delta(\lambda)$  and  $\varphi(\lambda)$  will have a similar shape, and the dependence of  $\omega(\lambda)$  will be close to a constant, which can be seen, for example, in Fig. 12d, where the value of the angle varies within two degrees in the entire range.

An important result of the performed analysis is that it is desirable to apply a double-sided antireflection coating to a quarter-wave achromatic polarization converter to reduce the interference effect. Taking the antireflection coating into account in the analysis consists of multiplying expression (31) on the left- and on the right-hand sides by a matrix of type (29), which describes this coating.

Figure 13a shows, as an example, transmittance of an achromatic quarter-wave plate for the wavelength range of 60–300  $\mu\text{m}$ , measured in [83] using a Vertex 70 Fourier spectrometer and calculated by the above method. A set of transmission spectra of an AWP placed between a pair of linear polarizers is considered. Each spectrum from the set corresponds to a certain angular position of the analyzer. One can see from the figure that the spread of transmittances for each position is within the signal-to-noise ratio of the Fourier spectrometer and, in this case, is approximately 1:100. This fact indicates that transmittance of such a system does not depend on the angular position of the analyzer, i.e., linearly polarized light is effectively converted into circularly polarized light in the specified range of 60–300  $\mu\text{m}$ .

The optical properties of the AWP given as an example were also investigated experimentally using optically pumped THz molecular lasers—a high-power pulsed  $\text{NH}_3$  laser at wavelengths of 90, 148, and 280  $\mu\text{m}$  and a continuous-wave methanol laser with a wavelength of 118  $\mu\text{m}$  [89–91].

Vertically polarized laser radiation transmitted through an achromatic quarter-wave plate was measured as a function of the rotation angle of the linear analyzer located after the AWP. The quarter-wave plate, fixed at the required angle between the direction of polarization of laser radiation and the optical axis, converts linear polarization into circular polarization. A typical experimental dependence of the signal on the analyzer angle (it rotated clockwise) is shown in Fig. 13b. The red circles show the signal of the linear analyzer in the absence of the AWP (wavelength of 148  $\mu\text{m}$ ). The red curve is the approxima-

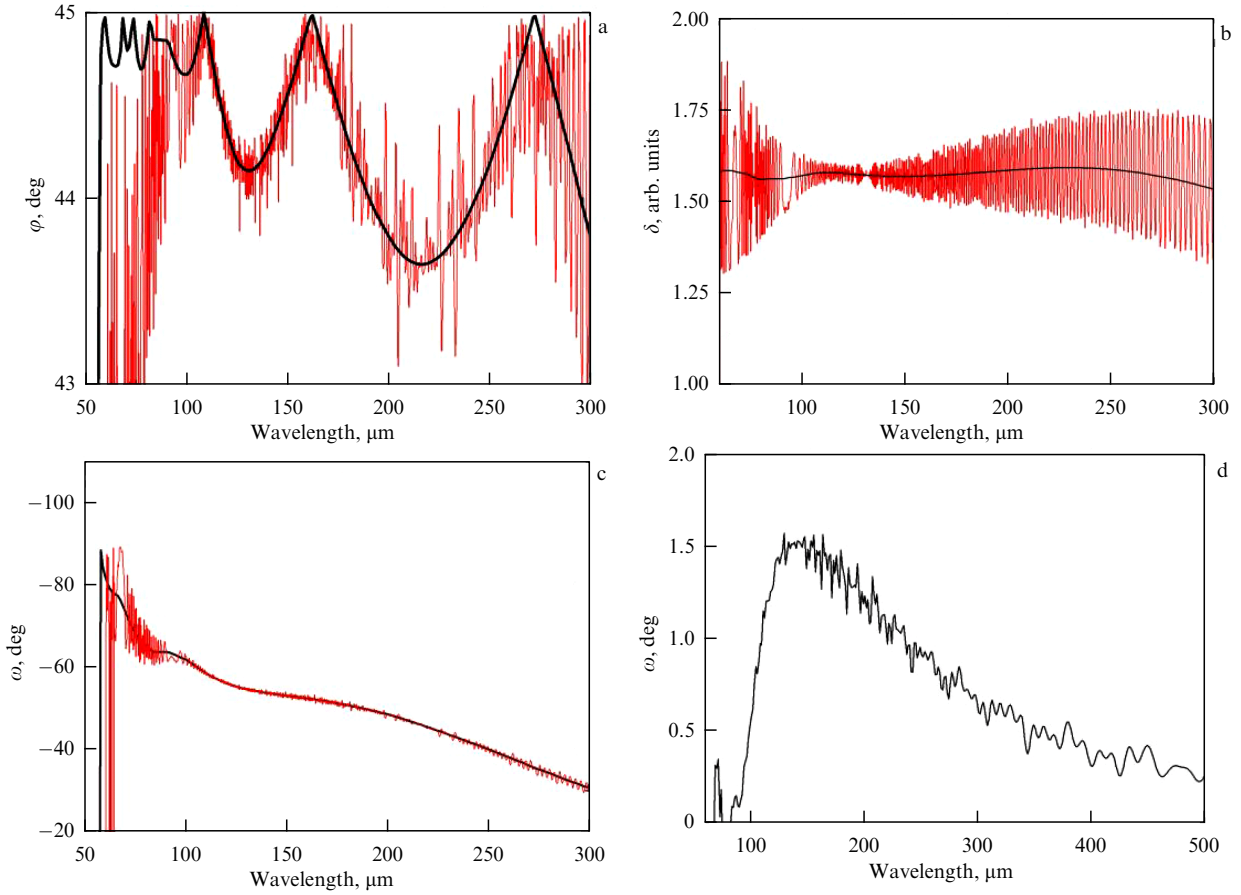


**Figure 12.** (a) Wavelength dependence of EOA angle  $\varphi$  when using a  $2 \times 2$  Jones matrix (black curve, without taking interference into account) and  $4 \times 4$  (red curve, taking interference into account). Calculations were performed for an AWP ( $\omega \neq \text{const}$ ) designed for an operating range of 60–300  $\mu\text{m}$ . (b) Dependence of rotation angle of effective rotator  $\omega(\lambda)$  for this AWP. (c) Dependence of retardation  $\delta(\lambda)$  for this AWP. (d) Example of dependence of  $\omega(\lambda)$  for an AWP designed for same operating range. (Borrowed from [83].)

tion of the analyzer function to the theoretical  $\cos^2 v$ , where  $v$  is the analyzer rotation angle. Blue diamonds show the signal in the presence of the AWP. One can see that the deviation of the AWP behavior from ideal is insignificant. For comparison, the same figure shows the dependence of the signal for a conventional monochromatic quarter-wave plate (triangles). One can see that, despite slightly higher light absorption, the quality of conversion into circular polarization is higher for the AWP. A certain degree of ellipticity (about 1%) can be attributed to experimental errors, such as imperfection of the polarizer.

As mentioned above, it is advisable to calculate the rotation angles and retardations of individual plates in the stack using simulated annealing. This algorithm is a probabilistic one that finds the optimal approximation of a system by a certain function as a result of an optimization search in the space of several variables. This function, which is also called the cost function, describes a complex system and depends on the detailed tuning of many parts of this system. When solving the problem of finding angles and retardations, the cost function is the value of radiation loss in the AWP and is described by the equation [82]

$$F = \sum_j (w_{\text{PD}}(\text{PD}_j - 90) + w_{\text{AX}}(\text{AX}_j - \text{AX}_1) + w_{\text{LI}}(\text{LI}_j - 0)). \quad (41)$$

In this equation, the phase difference PD, the optical axis AX, and the linearity LI are derived from the calculation of the eigenvalues and eigenvectors of the  $2 \times 2$  Jones matrix and depend on the wavelength. To obtain the AWP, the cost function  $F$  consists of the phase delay PD, the angle of the optical axis AX, and the degree of linearity LI at the output with specific weights  $w_{\text{PD}}$ ,  $w_{\text{AX}}$ , and  $w_{\text{LI}}$ , respectively. The value of the cost function is reduced by optimization in such a way that the sought variables are also reduced.

In the process of algorithm operation, a suitable composition of several quartz plates is found to minimize the value of the cost function that meets the established requirements for the phase delay (in paper [82], for example, a deviation of  $\pm 3^\circ$  is established), the region of deviation of the optical axes (ibid.,  $\pm 3^\circ$ ), and the degree of linearity at the output (ibid.,  $\pm 3^\circ$ ). The described algorithm is aimed at searching for a local minimum, and, unlike global search algorithms, it begins with an initial, randomly selected solution. Then, the ‘neighboring’ solution for this initial solution is calculated and the change in the cost function is estimated. If this change is in the opposite direction, the initial solution is replaced by the found generated ‘neighboring’ solution; otherwise, the original solution is preserved. This process is repeated until the cost function corresponding to the generated solution is within the predetermined criteria.

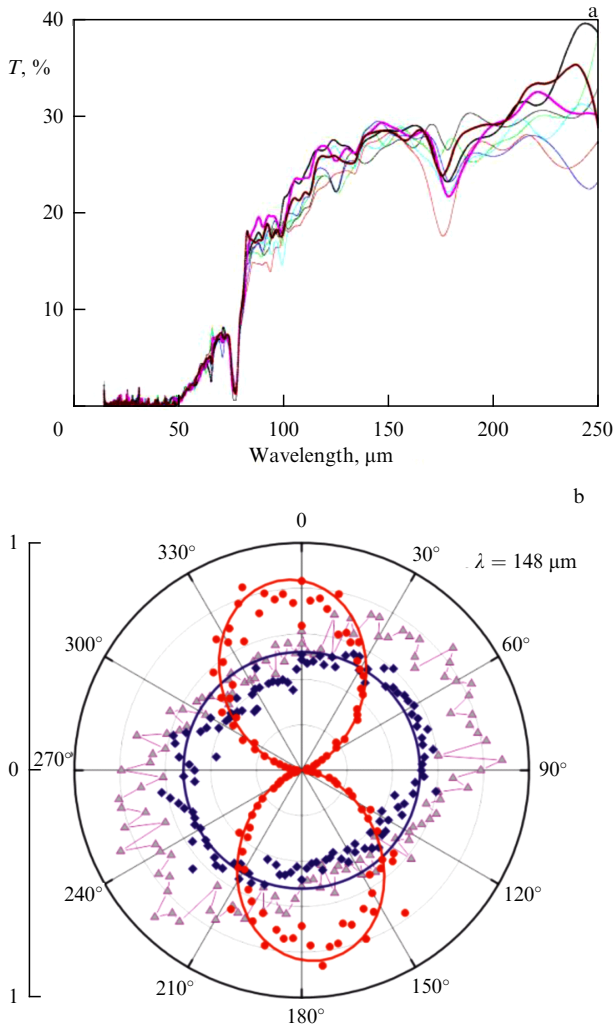


**Figure 13.** (a) Wavelength dependence of transmittance of linearly polarized light for a  $\lambda/4$  AWP for different analyzer angles (i.e., rotation angles of linear polarizer at AWP output). Curves are very similar. A small discrepancy between the curves is due to relatively low signal-to-noise ratio of spectrometer. (b) Laser radiation intensity without an AWP (red dots) and with an achromatic quarter-wave plate (blue diamonds) as a function analyzer rotation angle. Solid curves are ideal characteristics of analyzer (red) and AWP (blue). Triangles show dependence of signal when using a standard quarter-wave monochromatic plate at  $148 \mu\text{m}$ . (Borrowed from [83].)

### 3.2 Composite tunable phase-delay waveplates

Like achromatic polarization converters, composite tunable phase-delay waveplates (CWPs) are special stacks of identical plates made of the same material. Darsht [92] showed that a stack of three identical plates with the optical axes of birefringence of the outer plates oriented parallel is sufficient to ensure a possibility of controlled tuning of the phase plate to a certain wavelength with arbitrary retardation. The outer plates are oriented with their optical axes in the same way, with the azimuth of the optical axis of the middle plate relative to the azimuths of the outer ones being subject to calculation using a certain method. Then, the entire structure is oriented at a certain azimuthal angle relative to the azimuth of the electric vector of incident radiation. The value of this angle is obtained from the same calculation as the angle of mutual orientation of the plates in the stack. If the stack is assembled with a possibility of adjusting the orientation angles, i.e., without glue or contact, then it can be tuned to a number of

arbitrary wavelengths with sufficiently high accuracy, as is the case of both a quarter-wave and a half-wave plate. Composite phase plates serve as AWPs, but for a certain, not very wide, range of wavelengths (if we consider a stack of three WPs) — these are controlled phase plates, which are a converter (including a tunable one) of polarization, for example, rotation of the plane of polarization by an arbitrary angle. To expand the range of wavelengths, it is necessary, as for the case of AWPs in Section 3.1, to increase the number of plates in the stack.

To determine required retardation for a given wavelength in CWPs, Schneider et al. [89] first calculated the rotation angle  $\alpha$  of the middle plate using the formula

$$\alpha = 0.5 \arccos \left( \frac{\cos(\delta) \cos(\delta/2) - \cos(\delta_0/2)}{\sin(\delta) \sin(\delta/2)} \right), \quad (42)$$

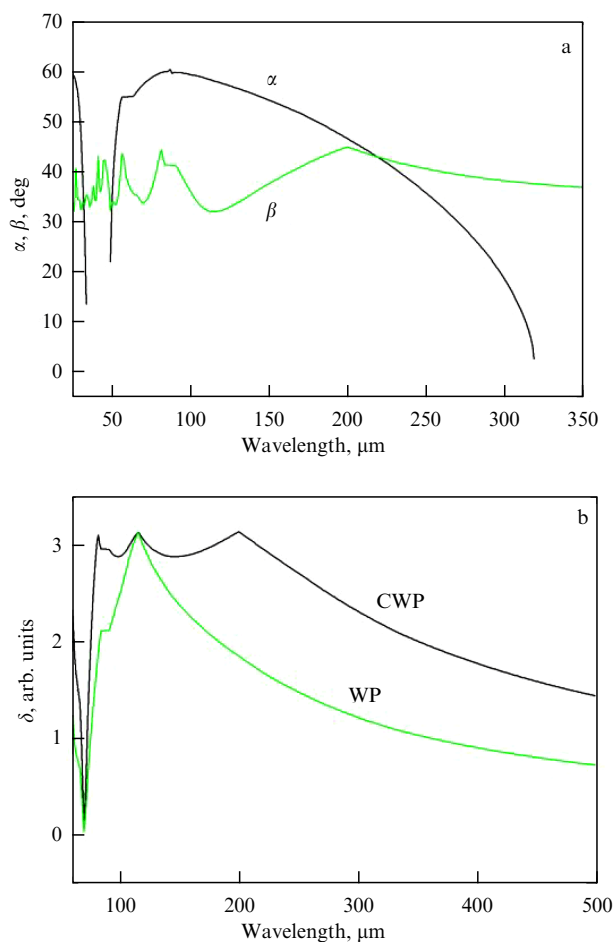
where  $\delta = 2\pi(n_o - n_e)d/\lambda$  (in the case of identical wave plates,  $\delta = \delta_1 = \delta_2 = \delta_3$ ), and  $\delta_0$  is the required retardation of the CWP. In this case, an acceptable plate thickness is selected to ensure CWP operation in the required wavelength range. The EOA rotation angle  $\beta$  of the CWP is calculated by substituting the found value of  $\alpha$  into formula (37), in which the elements of the matrix of type (33) are taken. Next, the interference corrections for these angles are determined. An example of the results of calculating a pair of these angles for a CWP with a retardation of  $\lambda/4$ , oriented to the operating range of  $60\text{--}300 \mu\text{m}$ , using  $2 \times 2$  Jones matrices, i.e., without taking into account interference corrections, is shown in Fig. 14a. Figure 14b also shows a comparison of the behavior of retardations for the described CWP at angles corresponding to a retardation of  $\lambda/4$  at a wavelength of  $118 \mu\text{m}$  and a monochromatic plate at a wavelength of  $118 \mu\text{m}$ . One can see that, at the specified wavelength, the CWP and a conventional monochromatic waveplate behave identically.

Figure 15 shows the results of a comparison of retardations for a tunable CWP and a monochromatic WP (borrowed from [93]). The figure also presents cases of (a) a half-wave plate and (b) a quarter-wave plate. It is evident that the same retardation values are achieved for the CWP and the monochromatic wave plate.

Examples of theoretical retardation dependences of  $\delta(\lambda)$ , calculated for the cases of Jones matrices  $2 \times 2$  and  $4 \times 4$ , are shown in Fig. 16 (the case of composite half-wave and quarter-wave plates). One can see that the general shape of the curves for different Jones matrices is the same, but the influence of interference leads to ‘noisiness’ of the curves at specific wavelengths.

Since a tunable waveplate assumes rotation of the middle plate relative to the outer ones, it is necessary to constructively provide an air gap between them. In this case, to calculate such a system using Jones matrices, in addition to matrices of type (10), it is necessary to introduce into the system two matrices of the type

$$\hat{Q}_0 = \begin{pmatrix} \cos\left(2\pi\frac{h}{\lambda_0}\right) & i \sin\left(2\pi\frac{h}{\lambda_0}\right) & 0 & 0 \\ i \sin\left(2\pi\frac{h}{\lambda_0}\right) & \cos\left(2\pi\frac{h}{\lambda_0}\right) & 0 & 0 \\ 0 & 0 & \cos\left(2\pi\frac{h}{\lambda_0}\right) & i \sin\left(2\pi\frac{h}{\lambda_0}\right) \\ 0 & 0 & i \sin\left(2\pi\frac{h}{\lambda_0}\right) & \cos\left(2\pi\frac{h}{\lambda_0}\right) \end{pmatrix}, \quad (43)$$



**Figure 14.** (a) Wavelength dependences of rotation angles of middle plate relative to outer ones ( $\alpha$ ) and of EOO of the system ( $\beta$ ), calculated for a CWP operating in range of 60–300  $\mu\text{m}$ . (b) Comparison of behavior of retardations for described CWP and a monochromatic plate at a wavelength of 118  $\mu\text{m}$ . (Borrowed from [83].)

describing the air gap. Here,  $h$  is the thickness of the air gap, and  $\lambda_0$  is the wavelength of the CWP operation. It should be noted that the need to provide an air gap significantly complicates the manufacture of such a device, since it is desirable to ensure as much parallelism as possible for all plates with a minimum air gap (units of  $\mu\text{m}$ ). In the case of a wedge-shaped gap, the calculation of this system by the Jones method is also possible if the wedge size is known, which is unlikely in practice. In this case, integration over small areas of plates corresponding to a specific gap size at a given point is introduced into the calculation.

As an example of the calculation, we can consider the case of conversion of linear polarization into circular polarization. The wavelength dependence of the fraction of linearly polarized light intensity  $I$  in total intensity is calculated, as is the case of an achromatic converter, using formula (34). The algorithm for finding the minimum of this value, as a function of a pair of angles ( $\alpha, \beta$ ) of the position of the optical axis of the middle plate relative to the outer ones and the rotation of the entire system as a whole, is as follows. A two-dimensional dependence of  $I(\alpha, \beta)$  is constructed, since all the values included in formula (34) depend on these angles. Then, a pair is found for which the value will be the smallest. Interference corrections for ( $\alpha, \beta$ ) due to the use of matrices of type (29), as opposed to matrices of type (33), can reach several degrees.

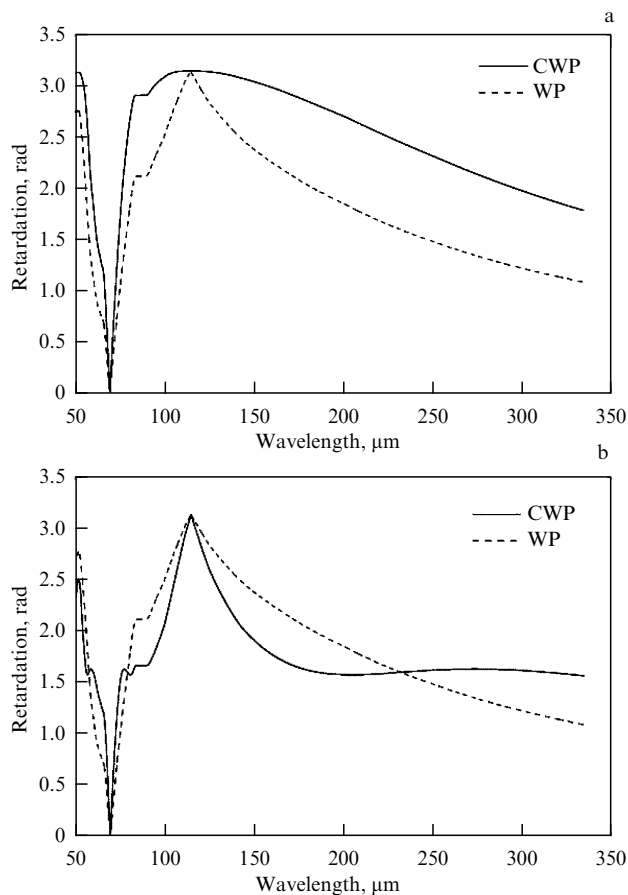


**Figure 15.** (a) Comparison of retardations of a tunable  $\lambda/2$  CWP at a wavelength of 120  $\mu\text{m}$  and a monochromatic WP at the same wavelength. (b) Comparison of retardations of a tunable  $\lambda/4$  CWP at a wavelength of 230  $\mu\text{m}$  and a monochromatic WP at the same wavelength (borrowed from [93]).

The method was experimentally tested using a Vertex 70 Fourier spectrometer and is described in [93]. This paper presents the results of comparing theoretically calculated and experimentally obtained transmission spectra of tunable  $\lambda/2$  and  $\lambda/4$  CWPs for wavelengths of 120 and 250  $\mu\text{m}$  and 220  $\mu\text{m}$ , respectively, located between two parallel linear polarizers. The theoretical transmittance was determined by multiplying the Jones matrix of the system by the matrices of the polarizers. It was shown that, in the wavelength ranges of 105–130 and 230–270  $\mu\text{m}$ , the transmittance of the  $\lambda/2$  CWP is close to zero, i.e., in these ranges, the considered CWP really served as a  $\lambda/2$  waveplate. For a  $\lambda/4$  CWP, the transmittance of the system was demonstrated to be independent of the angular position of the analyzer, i.e., linear polarization is really converted into circular in the specified range.

Note that the tuning range of the tunable CWP depends on the thickness of the stacked plates (and, of course, on the accuracy of retardation of individual waveplates) and, when use is made of 3–4 different sets, can cover the entire THz range. It should also be emphasized that a CWP allows polarization to be converted as a whole, i.e., not only from linear to circular and vice versa, but also between elliptical (with a given ratio of the axes and the angle between the axes of the input and output light).

All experimental results discussed in [93] demonstrate good agreement between theory and experiment. All experiments are consistent with the above theoretical model proposed on the basis of the CWP calculation, which allowed

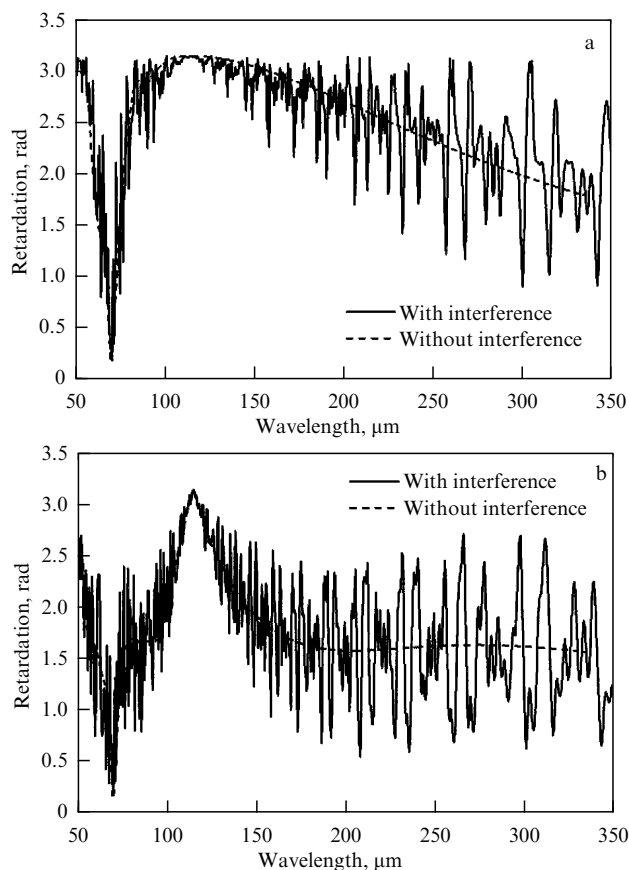


**Figure 16.** (a) Comparison of retardation of a  $\lambda/2$  CWP taking into account and not taking into account interference for a wavelength of 115  $\mu\text{m}$ . (b) Comparison of retardation of a  $\lambda/4$  CWP taking into account and not taking into account interference for a wavelength of 250  $\mu\text{m}$ . (Borrowed from [93].)

Tydex LLC [94] to calculate and manufacture commercial tunable CWPs in the THz range (Fig. 17a). Such CWPs have a clear aperture of at least 24 mm, the thickness of each of the WPs in the stack is 1.229 mm, and the distance between the plates is 3.19 or 2.81 mm, depending on the plate diameter. The operating range for half-wave and quarter-wave plates is 80–160  $\mu\text{m}$  and 150–300  $\mu\text{m}$ , respectively; when the plates are used as a Scholz filter (see description below), their operating range is 120  $\mu\text{m}$  at these fixed plate thicknesses.

In addition, a tunable CWP can be used as an achromatic waveplate in a small wavelength range. The theory of calculating AWP is described above in Section 3.1. Figure 17b shows a comparison of theoretical and experimental transmission spectra of a tunable CWP configured to operate as an AWP. One can see that this system in the wavelength range of 60–180  $\mu\text{m}$  can be used as an achromatic half-wave plate with a retardation accuracy of about  $\pm 5\%$ .

Zhang et al. [95] described an achromatic quarter-wave plate consisting of a quartz plate and an  $\text{MgF}_2$  plate operating in the IR range. Rosenberg [96] examined a similar converter for the THz wavelength range, and Zhang et al. [97] presented experimental results for a series of THz achromatic quarter-wave plates. The width of the spectral range in which the AWP stack operates is described by the value of the ‘frequency expansion factor’ (FE):  $\text{FE} = f_{\text{max}}/f_{\text{min}}$  (here,  $f_{\text{min}}$  is the frequency at which retardation deviation does not exceed 3%). The authors showed that there are two peculiar-

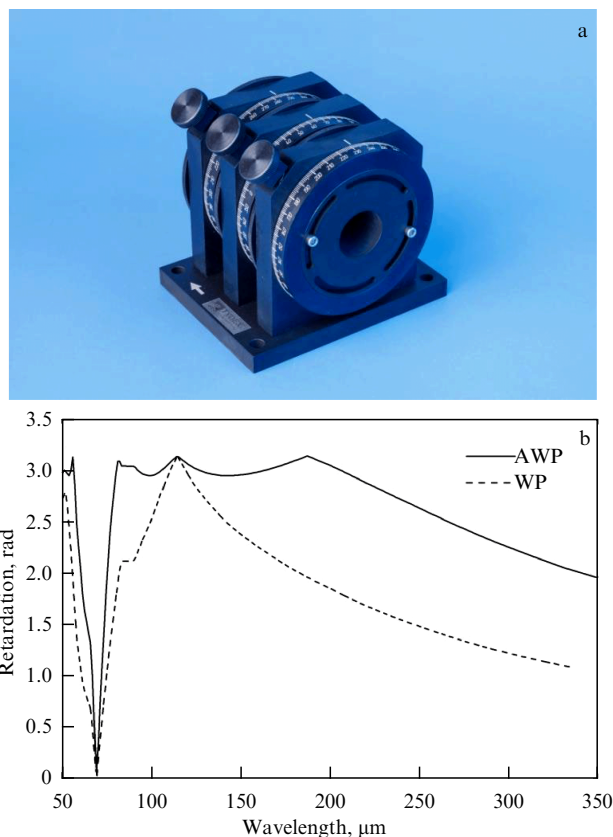


**Figure 17.** (a) Tunable CWP, manufactured by Tydex LLC [94]. (b) Comparison of theoretical and experimental transmission spectra of a tunable CWP tuned in AWP regime (borrowed from [93]).

ities in FE behavior: (i) FE is always equal to the number of monochromatic WPs in the stack, and (ii) the frequency range of AWP operation can be shifted by increasing the thickness of each plate in the stack by the same factor, according to the condition  $D_i = kd_i/f_{\text{min}}$ . These peculiarities were tested for stacks with FE varying from 2 to 6. The thicknesses and rotation angles of the plates were selected using simulated annealing. The experimental verification was performed on two AWP in the frequency range of 0.2–0.6 THz and 0.2–1.2 THz using a THz time-domain spectrometer. The spectrometer determined the ellipticity angles and transmittance of the  $\lambda/4$  AWP using three polarizers. Two photoconductive antennas were used as a THz emitter and a detector. The setup of the THz spectrometer is similar to that shown in Section 2 in Fig. 2a. Two measurements were performed for each AWP to determine the ellipticity angle. The analyzer was rotated by  $45^\circ$  or  $315^\circ$  relative to the orientation of the original polarization. The relationship between the measured electric fields in the time representation and the ellipticity angle  $\phi$  and retardation  $\delta$  can be calculated based on the fundamental formulas described above. Figure 18 shows, as an example, the measured and calculated ellipticity angle and retardation for a  $\lambda/4$  AWP in the 0.2–0.6-THz range taken from [97]. The oscillations in the figure are due to the interference effect.

It should be taken into account that too many plates in the stack are ineffective due to an increase in absorption of incident radiation. Thus, Chen et al. [82] described calculations using the Jones formalism for the spectral range of 1.3–1.8 THz for a  $\lambda/4$  AWP consisting of nine monochromatic waveplates stacked together. The simulated annealing algo-

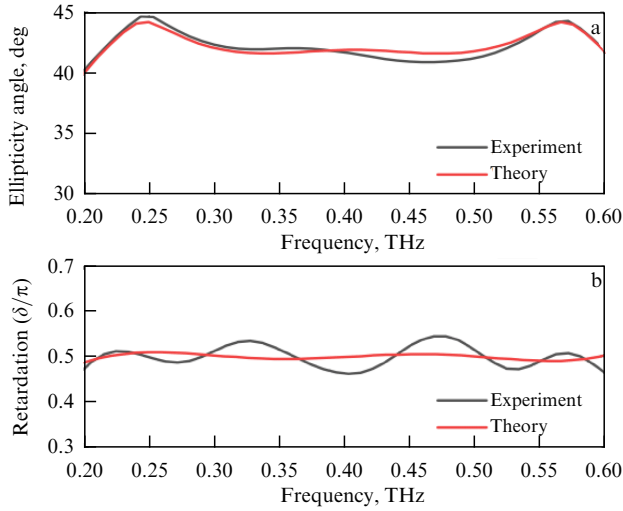


**Figure 18.** (a) Ellipticity angle (black line) of a  $\lambda/4$  AWP for range of 0.2–0.6 THz. Comparison with the model (red line) is also shown. (b) Retardation (black line) of a  $\lambda/4$  AWP for same range and comparison with the model (red line). (Borrowed from [97].)

rithm was also used in the calculation. As a result, the AWP showed good polarization parameters but had a low transmission rate.

Systems of birefringent plates with the optical axis of birefringence located in their plane can find another interesting application. For example, Kaveev et al. [93] showed that a system of three plates located between two crossed polarizers can serve as a terahertz spectrum analyzer.

The spectroscopic problem is generally formulated as follows [98]. Let a beam of light with an unknown spectral composition be incident on a system that is a nonselective (integrated) radiation receiver and a spectroscopic attachment. This attachment will be described by some hardware function  $K(\lambda, \gamma)$ , where  $\lambda$  is the radiation wavelength and  $\gamma$  is a generalized coordinate associated with control of the spectrometer. Examples of such systems include a Fabry–Perot interferometer with a hardware function [99] of the form  $K(\lambda, \gamma) \sim (1 + \cos(2\pi\gamma/\lambda))$  or a Michelson interferometer [100]. The solution to the spectroscopic problem is aimed at finding the spectral distribution of radiation incident on the system based on the response of the system with a known hardware function. Such a problem belongs to the class of ‘incorrect’ ones and involves solving the Fredholm equation of the first kind:

$$\int_{\lambda_1}^{\lambda_2} K(\lambda, \gamma) I(\lambda) d\lambda = F(\gamma). \quad (44)$$

It is necessary to reconstruct the original spectrum of the studied signal  $I(\lambda)$ , knowing the dependence of  $F(\gamma)$ , measured experimentally during the operation of the device. The limits of variation in  $\lambda$  and  $\gamma$  are known numbers. In this case, the Fredholm kernel is the hardware function. A similar problem is solved numerically, particularly by the regularization method, etc.

A system of quartz plates can be taken as a ‘spectroscopic attachment.’ It is shown that, for the best solution to the problem, it is sufficient to take three such plates, so that the outer plates in the stack have the same thickness, and the middle plate differs from the thickness of the outer ones by a

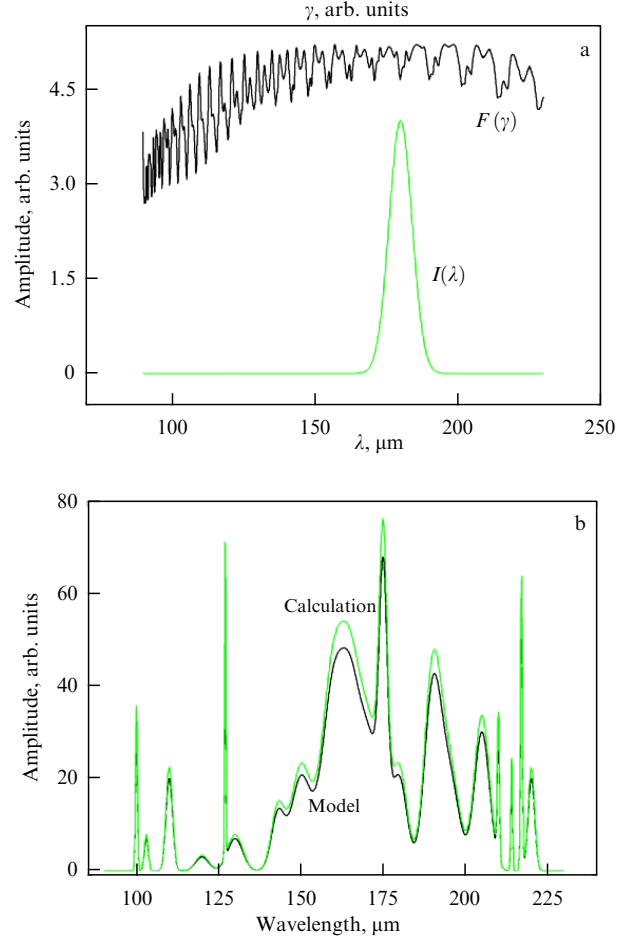


**Figure 19.** (a) Example of response, i.e., function  $F(\gamma)$ , to a known Gaussian-type function  $I(\lambda)$ . (b) Specified and calculated function  $I(\lambda)$ , which is a superposition of several peaks. In the absence of disturbances on right-hand side of equation, the function is reconstructed with good accuracy. (Borrowed from [83].)

factor of 0.8–1. Under these conditions, the rank of the matrix, which is the Fredholm kernel, is the highest.

The analytical expression for the Fredholm kernel of such a system is very cumbersome. This kernel is the transmittance of the system of quartz plates between two crossed polarizers, depending on the angles of rotation of the plates, which is equal to the square of the modulus of the off-diagonal component of the product of the Jones matrices, in the simplest case of form (33). Interference corrections to the kernel and taking into account the air layer that ensures the rotation of the plates are performed using the algorithm from Section 3.2, i.e., by multiplying matrices of form (29) and (43). An example of the functions  $I(\lambda)$  and  $F(\gamma)$  is shown in Fig. 19a (borrowed from [83]). In this case, the parameter  $\gamma$  is a certain generalized coordinate associated with the angles of rotation of the middle plate relative to the outer ones and the system as a whole. One can see from the figure that the kernel of the equation has a very complex form, as does the function  $F(\gamma)$ , with a fairly simple form of the function  $I(\lambda)$ .

The authors described the path of the numerical solution to a similar problem using known (model) functions  $F(\gamma)$ . After discretization of the equation, densely filled square matrices are obtained, which are ill-conditioned and unstable with respect to errors on the right-hand sides. One of the solution techniques is the global minimization method [101]

for the function  $I(\lambda)$ ; this function is a superposition of symmetric or asymmetric peaks (Fig. 19b) (borrowed from [83]), which is quite reasonable from the point of view of spectrum analysis. Physically based solutions were obtained after parameterization of the peaks by functions simulating the asymmetric peak using Edgeworth series [102]:

$$A(x) = A_G(x) + \sum_{k=3}^{\infty} (-1)^k \frac{\beta_k}{k!} A_G^{(k)}(x), \quad (45)$$

where  $A_G$  and  $A_G^{(k)}$  are the density function of the normal distribution and its derivatives, and  $\beta_k$  are quasi-moments, which are nonlinearly expressed through the cumulants  $K_n$ . The parameters of the Edgeworth series were considered to be the cumulant coefficients  $\gamma_n = K_n/K_2^{n/2}$ . In particular,  $\gamma_3 = K_3/K_2^{3/2}$  is the peak asymmetry coefficient and  $\gamma_4 = K_4/K_2^2$  is the excess coefficient (characterizes the deviation of the distribution from the Gaussian towards a more or less sharp peak). Next, the final Edgeworth series was considered taking into account the variable cumulant coefficients  $\gamma_1, \gamma_2, \dots, \gamma_{10}$ . The optimal values of these coefficients were found using the least squares method:

$$F = \sum (Y_i^{\text{experm}} - Y_i^{\text{theor}})^2 \rightarrow \min. \quad (46)$$

It was found that the functional  $F$  is multi-extremal; therefore, the fundamental point was to use the method of global search for the minimum of the functional [101]. An increase in the stability of the solution to perturbations of the function  $F(\gamma)$ , arising under the conditions of a real spectrum analysis experiment, is proposed by using the Tikhonov regularization method, which considers the problem of minimizing a parametric functional of the form

$$\Phi_x(A, \tilde{b}, x) = \|Ax - \tilde{b}\|_2^2 + \alpha^2 \|Lx\|_2^2, \quad (47)$$

where  $\alpha$  is the regularization parameter,  $\tilde{b}$  is the realization of the right-hand-side vector with random perturbations,  $x$  is the regularized solution to the problem, and  $L$  is the discrete first-order differentiation operator

$$L = \begin{pmatrix} 1 & -1 & 0 & \dots & 0 & 0 \\ 0 & 1 & -1 & \dots & 0 & 0 \\ \dots & \dots & \dots & \dots & \dots & \dots \\ 0 & 0 & 0 & \dots & 1 & -1 \end{pmatrix}. \quad (48)$$

Based on [98, 103], the authors choose the parameter

$$\alpha^2 = \frac{\delta \times \sigma_{\max}^2(A)}{\|\tilde{b}\|_2 + \delta},$$

assuming that the matrix  $A$  is specified exactly and the perturbations of the problem are determined only by perturbations of the right-hand side vector  $b$ , where  $\|\tilde{b} - b\| \leq \delta$ , and  $\sigma_{\max}(A)$  is the maximum singular value of the matrix  $A$ . Minimization of the Tikhonov functional was carried out using the method of extended regularized systems [104]. Kaveev et al. [83] managed to obtain physically justified solutions, but their accuracy at the time of publication of their paper did not allow the results to be used for practical purposes.

**3.3 Terahertz polarization filters**

Numerous papers are devoted to various polarization filters in the IR and visible ranges [105–121]. These filters were

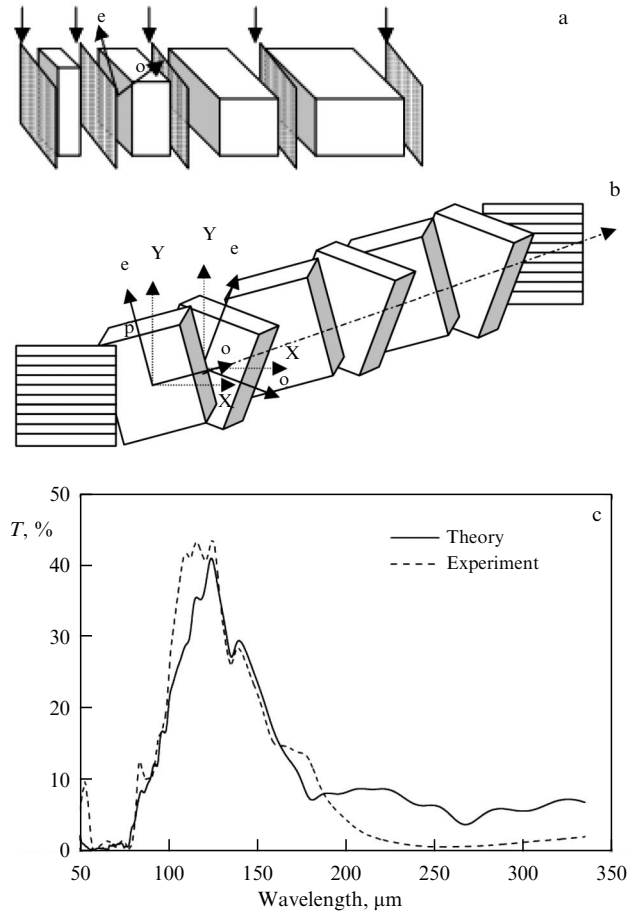


**Figure 20.** (a) Example of Lyot filter (borrowed from [110]). (b) Folded Scholz filter (borrowed from [124]). (c) Theoretical and experimental transmission spectra of a tunable CWP tuned in Scholz filter regime for a wavelength of 125 μm (borrowed from [93]).

developed several decades ago. However, their adaptation for the THz wavelength range has begun relatively recently. Two main types of composite polarization filters are known: Scholz and Lyot [85]. Lyot filters were developed in the 1930s–1940s and consist of a sequence of WPs of different thicknesses and linear polarizers (Fig. 20a).

Scholz filters consist of a stack of identical phase plates (folded arrangement) with equal but opposite signs, azimuthal angles  $\rho$  of the optical axes between crossed polarizers (folded Scholz filter, the angle of the  $k$ th polarizer is  $\phi_k = (-1)^k \rho, k = 0, 1, \dots$ ), or (fan arrangement) with successive rotation by the same azimuthal angle of the optical axes of the polarizers (fan Scholz filter,  $\phi_k = (2k + 1)\rho, k = 0, 1, \dots$ ). The Scholz filter is inferior to the Lyot filter in suppressing secondary maxima near the passband. At the same time, its passband is somewhat narrower, and transmittance is higher [108]. Scholz filters can be made tunable by using active controlled WPs, such as electro-optical waveplates [122] or liquid crystal waveplates [123].

The folded Scholz filter [124] (Fig. 20b) consists of a pile of an even number of half-wave plates for frequency  $f_c$ , with only two crossed polarizers, one at each end. Each of the waveplates is alternately oriented at an azimuthal angle  $\rho$  and  $-\rho$  relative to the direction of polarization of the incident electromagnetic wave. The calculation of the Scholz filter is described, for example, in [85]. The center frequency  $f_c$  of the

filter is determined by the expression

$$f_c = \frac{(2m+1)c}{2(n_e - n_o)d}, \quad m = 0, 1, 2, 3, \dots, \quad (49)$$

where  $n_o$  and  $n_e$  are the refractive indices of ordinary and extraordinary waves, respectively;  $d$  is the thickness of each waveplate;  $m$  is the order of the half-wave plate; and  $c$  is the speed of light in a vacuum. Using the Jones matrix method and the Chebyshev identity [125], transmittance of the Scholz filter can be written as

$$T = \left| \tan(2\rho) \cos \chi \frac{\sin(N\chi)}{\sin \chi} \right|^2. \quad (50)$$

In equation (50),  $\cos \chi = \cos(2\rho) \sin(\Gamma/2)$ , where  $\Gamma$  is the frequency-dependent retardation of each plate, and  $N$  is an even number of plates. In addition, equation (50) reduces to  $T = \sin^2(2N\rho)$  at  $\Gamma = (2m+1)\pi$ . Thus, transmittance of the filter at  $f_c$  is 100% if  $\rho = \pi/4N$ .

Ho et al. [126] described a composite THz Scholz filter based on two controlled liquid crystal waveplates sandwiched between two parallel wire grid polarizers and demonstrated transmittance of this filter in the 0.176–0.793-THz band.

Chen et al. [127] demonstrated a tunable THz Lyot filter in the frequency range from 0.388 to 0.564 THz, also based on liquid crystal waveplates.

The calculation of birefringent polarization filters by using the Jones formalism was developed in a number of papers (see, for example, [108, 109, 112, 118, 120, 121, 128–130]) and in dozens of other works. At the same time, most of the experimentally designed Scholz filters operated outside the THz wavelength range.

Experiments [93] showed that a CWP (it is convenient to use a tunable waveplate) can serve as a Scholz filter in the case of a certain choice of the angular position of the plates. The angles in this case are +15, –15, and +15 (due to the crossed Scholz filter)—they were calculated based on the theory described in [128]. There is no way to tune the filter passband, since it depends on the thickness of the plates in the stack. To operate the filter in this regime, it is necessary to place a CWP between crossed linear polarizers. Figure 20c shows a comparison of the theoretical and experimental transmission spectra of this system. The system is a Scholz filter with a wavelength of 125  $\mu\text{m}$ . One can see that the experiment agrees very well with the theory. A small discrepancy between the curves is due to the relatively low signal-to-noise ratio of the spectrometer in the wavelength range in question.

## 4. Conclusions

The review considered devices that convert polarization of THz radiation—from simple elementary converters to more complex combined apparatuses—and have demonstrated that there are a number of papers devoted to THz polarization devices, including exotic ones based on metamaterials, graphene, etc. However, quartz polarization optics devices are most widely used due to their versatility and relative ease of manufacture. It was shown experimentally shown that it is possible to adjust a tunable composite quartz waveplate to different polarization conversion patterns: as a quarter-wave or half-wave (or with another specified phase) plate in a wide range of wavelengths. Such waveplates can also be used as a Scholz bandpass filter. THz polarimetry is an integral part of

THz spectroscopy for a complete analysis of THz radiation characteristics. This area of optics will continue to develop.

On the basis of the above review, further development of THz polarization optics may be associated with improving the quality of manufactured devices and components: the accuracy of manufacturing quartz and sapphire plates with regard to the angle relative to crystallographic axes, the quality and accuracy of wire winding, and increasing the polarizer aperture size to hundreds of millimeters in diameter for wire grid polarizers. Improving the characteristics of tunable polarization converters may be associated with increasing mechanical accuracy of plate holders, which will allow the width of air gaps between the plates to be significantly, if not completely, reduced. The algorithms for calculating polarization optics are well known and well developed, and it is unlikely that they will need improvement. In order to improve the characteristics (degree of polarization, size, spectrum width), work on exotic polarization conversion devices will continue, but they are unlikely to have commercial significance in the nearest future.

## References

1. Federici J F et al. *Semicond. Sci. Technol.* **20** S266 (2005)
2. Friederich F et al. *IEEE Trans. Terahertz Sci. Technol.* **1** 183 (2011)
3. Ajito K, Ueno Y *IEEE Trans. Terahertz Sci. Technol.* **1** 293 (2011)
4. Humphreys K et al., in *The 26th Annual Intern. Conf. of the IEEE Engineering in Medicine and Biology Society, San Francisco, CA, USA, 2004*, p. 1302, <https://doi.org/10.1109/IEMBS.2004.1403410>
5. Zhang X-C, Xu J *Introduction to THz Wave Photonics* (New York: Springer-Verlag, 2010) pp. 49–52, [https://doi.org/10.1007/978-1-4419-0978-7\\_3](https://doi.org/10.1007/978-1-4419-0978-7_3)
6. Taylor Z D et al. *IEEE Trans. Terahertz Sci. Technol.* **1** 201 (2011)
7. Nuss M C, Orenstein J, in *Millimeter and Submillimeter Wave Spectroscopy of Solids* (Topics in Applied Physics, Vol. 74, Eds G Grüner) (Berlin: Springer, 2007) p. 7, <https://doi.org/10.1007/BFb0103419>
8. Gong Y et al. *Microw. Opt. Technol. Lett.* **63** 1605 (2021)
9. Bréhat F, Wyncke B *Int. J. Infrared Millimeter Waves* **18** 1663 (1997)
10. Zubair A et al. *Appl. Phys. Lett.* **108** 141107 (2016)
11. Kyoung J et al. *Nano Lett.* **11** 4227 (2011)
12. Anjali, Varshney R, Kumar S J. *Opt. Soc. Am. B* **40** 1688 (2023)
13. Zaman A M et al. *Front. Nanotechnol.* **5** 1 (2023) <https://doi.org/10.3389/fnano.2023.1057422>
14. Yan F et al. *J. Infrared Millimeter Terahertz Waves* **34** 489 (2013)
15. TYDEX. THz Film Polarizers, [https://www.tydexoptics.com/products/thz\\_polarizers/thz\\_polarizers1/](https://www.tydexoptics.com/products/thz_polarizers/thz_polarizers1/)
16. Vickers D G, Robson E I, Beckman J E *Appl. Opt.* **10** 682 (1971)
17. Martin D H, Puplett E *Infrared Phys.* **10** 105 (1970)
18. Costley A E et al. *J. Opt. Soc. Am.* **67** 979 (1977)
19. Sentz A et al. *Rev. Sci. Instrum.* **49** 926 (1978)
20. Shapiro J B, Bloemhof E E *Int. J. Infrared Millimeter Waves* **11** 973 (1990)
21. Hu Y et al. *J. Aerospace Eng.* **233** 1916 (2019) <https://doi.org/10.1177/0954410018791888>
22. TYDEX. THz Wire Grid Polarizers, [https://www.tydexoptics.com/products/thz\\_polarizers/thz\\_polarizers/](https://www.tydexoptics.com/products/thz_polarizers/thz_polarizers/)
23. Moon S, Kim D J. *Opt. Soc. Am. A* **23** 199 (2006)
24. Liao Y-L, Zhao Y *Opt. Quantum Electron.* **46** 641 (2014)
25. Lalanne P, Hugonin J-P *J. Opt. Soc. Am. A* **15** 1843 (1998)
26. Haggans C W, Li L, Kostuk R K *J. Opt. Soc. Am. A* **10** 2217 (1993)
27. Kim D, Burke K *Appl. Opt.* **42** 6321 (2003)
28. Thurman S T, Morris G M *Appl. Opt.* **42** 3225 (2003)
29. Chen C, Lu Z, Zhao B *Proc. SPIE* **4223** 101 (2000)
30. Boedecker G, Henkel C *Opt. Express* **11** 1590 (2003)
31. Koschny T et al. *Phys. Rev. Lett.* **93** 107402 (2004)
32. Li L *J. Opt. Soc. Am. A* **13** 1870 (1996)
33. Dai M et al. *Opt. Express* **23** 15390 (2015)
34. Gorelik G S *Kolebaniya i Volny: Vvedenie v Akustiku, Radiofiziku i Optiku* (Oscillations and Waves: Introduction to Acoustics, Radio-physics, and Optics) (Moscow: Fizmatgiz, 1959)

35. Dorn R, Quabis S, Leuchs G *J. Mod. Opt.* **50** 1917 (2003)
36. Dorn R, Quabis S, Leuchs G *Phys. Rev. Lett.* **91** 233901 (2003)
37. Quabis S et al. *Opt. Commun.* **179** 1 (2000)
38. Hall D G *Opt. Lett.* **21** 9 (1996)
39. Zhan Q *Adv. Opt. Photon.* **1** 1 (2009)
40. Gori F, Guattari G, Padovani C *Opt. Commun.* **64** 491 (1987)
41. Quabis S, Dorn R, Leuchs G *Appl. Phys. B* **81** 597 (2005)
42. Novotny L, Hecht B *Principles of Nano-Optics* (Cambridge: Cambridge Univ. Press, 2006)
43. Maekawa A, Uesaka M, Tomizawa H, in *Proc. of the 30th Intern. Free Electron Laser Conf., FEL08, Gyeongju, Korea*, pp. 435–438; <https://jacow.org/FEL2008/papers/TUPPH082.pdf>
44. Machavariani G et al. *Opt. Commun.* **281** 732 (2008)
45. TYDEX. THz Waveplates, [https://www.tydexoptics.com/products/thz\\_polarizers/thz\\_waveplate/](https://www.tydexoptics.com/products/thz_polarizers/thz_waveplate/)
46. Wikipedia. Wollaston prism, [https://en.wikipedia.org/wiki/Wollaston\\_prism](https://en.wikipedia.org/wiki/Wollaston_prism)
47. Azimuth Photonics, Thorlabs' Wollaston prisms, <https://azimp.ru/thorlabs/wollaston-polarizer/>
48. StudFiles. St. Petersburg State Univ. of Information Technologies, Mechanics and Optics. Laboratory work No. 16 “Opređenje koncentracije rastvora sakhara s pomoshch'yu poljarimetra” (“Measuring the concentration of sugar solution with a polarimeter”), <https://studfile.net/preview/6074976/>
49. Bennett J M, in *Handbook of Optics* (Ed. in Chief M Bass) 2nd ed. (New York: McGraw-Hill, 1995) pp. 3.13–3.14
50. Archard J F, Taylor A M *J. Sci. Instrum.* **25** 407 (1948)
51. Wikipedia. Glan–Taylor prism, [https://en.wikipedia.org/wiki/Glan%E2%80%93Taylor\\_prism](https://en.wikipedia.org/wiki/Glan%E2%80%93Taylor_prism); <https://commons.wikimedia.org/wiki/File:Glan-foucault.png?uselang=ru>
52. Fan J-Y, Li H-X, Wu F-Q *Opt. Commun.* **223** 11 (2003)
53. Vardaxoglou J C *Frequency Selective Surfaces: Analysis and Design* (Electronic and Electrical Engineering Research Studies. Antennas Ser., Vol. 10) (Taunton: Research Studies Press, New York: J. Wiley, 1997)
54. Munk B A *Frequency Selective Surfaces: Theory and Design* (New York: John Wiley, 2000)
55. Wu T-K, in *Encyclopedia of RF and Microwave Engineering* (Ed. K Chang) (Hoboken, NJ: John Wiley, 2005)
56. Suresh Kumar N et al. *Crystals* **11** 518 (2021)
57. Yen T J et al. *Science* **303** 1494 (2004)
58. Moser H O et al. *Phys. Rev. Lett.* **94** 063901 (2005)
59. Peralta X G et al. *Opt. Express* **17** 773 (2009)
60. Pisano G et al. *Appl. Opt.* **55** 10255 (2016)
61. Acuna G et al. *Opt. Express* **16** 18745 (2008)
62. Strikwerda A C et al. *Opt. Express* **17** 136 (2009)
63. Masson J-B, Gallot G *Opt. Lett.* **31** 265 (2006)
64. Zhang X et al. *Opt. Mater. Express* **10** 282 (2020)
65. Cong L et al. *Laser Photon. Rev.* **8** 626 (2014)
66. Kawada Y et al. *Opt. Lett.* **39** 2794 (2014)
67. Nagai M et al. *Opt. Lett.* **39** 146 (2014)
68. Kanda N, Konishi K, Kuwata-Gonokami M *Opt. Express* **15** 11117 (2007)
69. Hsieh C-F et al. *Opt. Lett.* **31** 1112 (2006)
70. Tsai T-R et al. *Appl. Opt.* **42** 2372 (2003)
71. Pan R-P et al. *Mol. Cryst. Liquid Cryst.* **409** 137 (2004)
72. Chen C-Y et al. *Appl. Phys. Lett.* **83** 4497 (2003)
73. Chen C-Y et al. *Opt. Express* **12** 2625 (2004)
74. Tsai T-R et al. *IEEE Microwave Wireless Comp. Lett.* **14** 77 (2004)
75. Zhang B, Gong Y *Opt. Express* **23** 14897 (2015)
76. Drysdale T D et al. *Electron. Lett.* **37** 149 (2001)
77. Drysdale T D et al. *IEEE Trans. Antennas Propag.* **51** 3072 (2003)
78. Savini G, Pisano G, Ade P A R *Appl. Opt.* **45** 8907 (2006)
79. Pancharatnam S *Proc. Indian Acad. Sci.* **41** 130 (1955)
80. Ma J et al. *Chin. J. Astron. Astrophys.* **8** 349 (2008)
81. Kang G et al. *Opt. Express* **18** 1695 (2010)
82. Chen Z et al. *Opt. Commun.* **311** 1 (2013)
83. Kaveev A K et al. *Appl. Opt.* **52** B60 (2013)
84. TYDEX. THz Broad-Band Phase Transformers, [https://www.tydexoptics.com/products/thz\\_polarizers/thz\\_converters/](https://www.tydexoptics.com/products/thz_polarizers/thz_converters/)
85. Yariv A, Yeh P *Optical Waves in Crystal: Propagation and Control of Laser Radiation* (New York: John Wiley and Sons, 1984) pp. 132–158
86. Clark Jones R *J. Opt. Soc. Am.* **31** 488 (1941)
87. Kirkpatrick S, Gelatt C D (Jr.), Vecchi M P *Science* **220** 671 (1983)
88. Press W H et al. *The Art of Scientific Computing* (Cambridge: Cambridge Univ. Press, 1997)
89. Schneider P et al. *J. Appl. Phys.* **96** 420 (2004)
90. Kvon Z-D et al. *Physica E* **40** 1885 (2008)
91. Ganichev S, Prettl W *Intense Terahertz Excitation of Semiconductors* (Oxford: Oxford Univ. Press, 2006) <https://doi.org/10.1093/acprof:oso/9780198528302.001.0001>
92. Darsh M “Vliyanie sredy i vneshnikh vozdeistvii na rasprostraneniye polarizovannogo sveta” (“Effect of a medium and external influences on propagation of polarized light”), PhD Thesis (Phys.-Math. Sci.) (Chelyabinsk: Chelyabinsk State Technical Univ., 1996)
93. Kaveev A K et al. *Appl. Opt.* **53** 5410 (2014)
94. TYDEX. Tunable THz Polarization Converter, [https://www.tydexoptics.com/products/thz\\_polarizers/tunable\\_thz\\_polarization\\_converter/](https://www.tydexoptics.com/products/thz_polarizers/tunable_thz_polarization_converter/)
95. Zhang T, Popov D, Khodzitsky M, in *Proc. of the 46th Intern. Conf. on Infrared, Millimeter and Terahertz Waves, IRMMW-THz, 29 August 2021–03 September 2021, Chengdu, China*, <https://doi.org/10.1109/IRMMW-THz50926.2021.9567029>
96. Rosenberg W J, Title A M *Proc. SPIE* **0307** 120 (1982)
97. Zhang T, Kropotov G, Khodzitsky M *Opt. Continuum* **2** 1597 (2023)
98. Tikhonov A N, Arsenin V Ya *Solutions of Ill-Posed Problems* (Washington, DC: Halsted Press, 1977); Translated from Russian: *Metody Resheniya Nekorrektnykh Zadach* (Moscow: Nauka, 1979)
99. Zhiglinskii A G, Kuchinskii V V *Real'nyi Interferometr Fabry–Pero* (Real Fabry–Perot Interferometer) (Moscow: Mashinostroeniye, 1983)
100. Ikram M, Hussain G *Appl. Opt.* **38** 113 (1999)
101. Deyanov R Z, Shchedrin B M *Prikl. Matem. Inform.* (30) 46 (2008)
102. Malakhov A N *Kumulyantnyi Analiz Sluchainykh Negaussovykh Protsessov i ikh Preobrazovaniy* (Cumulant Analysis of Random Non-Gaussian Processes and Their Transformations) (Moscow: Soviet Radio, 1978)
103. Tikhonov A N, Samarskii A A *Equations of Mathematical Physics* (Oxford: Pergamon Press, 1990) translated from 5th Russian ed.; *Urvneniya Matematicheskoi Fiziki* 7th ed. (Moscow: Nauka, 2004)
104. Zhdanov A I *Comput. Math. Math. Phys.* **52** 194 (2012); *Zh. Vychisl. Matem. Matem. Fiz.* **52** 205 (2012)
105. Bloom A L *J. Opt. Soc. Am.* **64** 447 (1974)
106. Kobtsev S M *Opt. Spectrosc.* **63** 672 (1987); *Opt. Spektrosk.* **63** 1139 (1987)
107. Lee Y L et al. *Opt. Lett.* **32** 2813 (2007)
108. Evans J W *J. Opt. Soc. Am.* **48** 142 (1958)
109. Zhou Y et al. *J. Opt. Soc. Am. A* **20** 733 (2003)
110. Shabtay G et al. *Opt. Express* **10** 1534 (2002)
111. Yang X et al. *J. Opt. Soc. Am. A* **22** 752 (2005)
112. Wang X, Yao J *Appl. Opt.* **31** 4505 (1992)
113. Preuss D R, Gole J L *Appl. Opt.* **19** 702 (1980)
114. Mentel J, Schmidt E, Mavrudis T *Appl. Opt.* **31** 5022 (1992)
115. Title A M *Appl. Opt.* **15** 2871 (1976)
116. von Willisen F K *Appl. Opt.* **5** 97 (1966)
117. Title A M *Appl. Opt.* **14** 445 (1975)
118. Melich R, Melich Z, Šolc I *Proc. SPIE* **7018** 701854 (2008)
119. Melich R, Melich Z, Šolc I, in *The Physics of Chromospheric Plasmas* (ASP Conf. Ser., Vol. 368, Eds P Heinzel, I Dorotović, R J Rutten) (San Francisco, CA: Astronomical Society of the Pacific, 2007) p. 621
120. Yu X J et al. *Displays* **23** 145 (2002)
121. Yeh P *Opt. Commun.* **29** 1 (1979)
122. Pinnow D A et al. *Appl. Phys. Lett.* **34** 391 (1979)
123. Tarry H A *Electron. Lett.* **11** 471 (1975)
124. Šolc I *J. Opt. Soc. Am.* **55** 621 (1965)
125. Vasil'ev N, Zelevinskii A “Mnogochleny Chebysheva i rekurentnyye sootnosheniya” (“Chebyshev polynomials and recurrence relations”) *Kvant* (1) 12 (1982)
126. Ho I-C et al. *Opt. Lett.* **33** 1401 (2008)
127. Chen C-Y et al. *Appl. Phys. Lett.* **88** 101107 (2006)
128. Ghosh A, Chakraborty A K *Opt. Acta* **29** 1407 (1982)
129. Jung H *Int. J. Opt. Hindawi* **2010** 1 (2010) <https://doi.org/10.1155/2010/626583>
130. Hong H-G et al. *Opt. Express* **17** 15455 (2009)